Structural relationships and a phase diagram for $(Ca,Sr)TiO_3$ perovskites

2006 J. Phys.: Condens. Matter 18 10725

(http://iopscience.iop.org/0953-8984/18/48/002)

INSTITUTE OF PHYSICS PUBLISHING JOURNAL OF PHYSICS: CONDENSED MATTER

J. Phys.: Condens. Matter **18** (2006) 10725–10749 doi:10.1088/0953-8984/18/48/002

Structural relationships and a phase diagram for (Ca, Sr)TiO_3 perovskites

M A Carpenter[1], C J Howard[2], K S Knight[3] and Z Zhang[2]

[1] Department of Earth Sciences, University of Cambridge, Downing Street, Cambridge CB2 3EQ, UK
[2] Australian Nuclear Science and Technology Organisation, Private Mail Bag 1, Menai, NSW 2234, Australia
[3] ISIS Facility, Rutherford Appleton Laboratory, Chilton, Didcot, Oxfordshire OX11 0QX, UK

Received 31 July 2006, in final form 26 September 2006
Published 17 November 2006
Online at stacks.iop.org/JPhysCM/18/10725

Abstract

Sets of lattice parameter data have been obtained from high resolution neutron and synchrotron x-ray powder diffraction patterns collected *in situ* as a function of temperature for perovskites in the (Ca, Sr)TiO_3 solid solution. An updated phase diagram is proposed in which there is a stability field for the $I4/mcm$ structure at all compositions across the solid solution. The $Pm\bar{3}m \leftrightarrow I4/mcm$ transition is close to tricritical in the composition range 0–70% $SrTiO_3$ component and then evolves towards second order character (Landau 246 solution) in the range 85–100% $SrTiO_3$. Transition temperatures as a function of composition for $I4/mcm \leftrightarrow Pnma$ and $I4/mcm \leftrightarrow Pbcm$ transitions at lower temperatures show a break in slope at ∼60% $SrTiO_3$. Variations of octahedral tilt angles and spontaneous strains are much the same for $Pbcm$ structures as they are for $Pnma$ structures. Nearly cubic lattice geometry of orthorhombic structures at intermediate compositions is ascribed to only weak coupling between octahedral tilting and the shear strain e_4. The phase diagram topology and variations in structural evolution at different compositions indicate that there is a distinct change in the behaviour of the solid solution at ∼85% $SrTiO_3$.

1. Introduction

$CaTiO_3$, the original natural perovskite named after Count L V Perovskii, is linked to $SrTiO_3$, one of the most widely utilized man-made perovskites, via a continuous solid solution which displays coupled phase transitions. $CaTiO_3$ (CST0) itself undergoes two transitions at high temperatures associated with octahedral tilting. The currently accepted sequence of symmetry changes is $Pm\bar{3}m \leftrightarrow I4/mcm \leftrightarrow Pnma$ (Redfern 1996, Ali and Yashima 2005), and the most recent temperature determination has these placed at 1634 ± 13 and 1498 ± 25 K, respectively (Ali and Yashima 2005). In contrast, $SrTiO_3$ (CST100) undergoes a single

$Pm\bar{3}m \leftrightarrow I4/mcm$ tilting transition at ~105 K (Unoki and Sakudo 1967, Shirane and Yamada 1969, Cowley *et al* 1969, Worlock *et al* 1969, Müller and Berlinger 1971). Intermediate members of the (Ca, Sr)TiO_3 (CST) solid solution display combined tilting, antiferroelectric and ferroelectric instabilities (Mitsui and Westphal 1961, Bednorz and Müller 1984, Ceh *et al* 1987, Hirata *et al* 1996, Lemanov 1997, Ball *et al* 1998, Ranjan and Pandey 1999, 2001a, 2001b, Ranjan *et al* 1999, 2000, 2001, Qin *et al* 2000, 2002, Carpenter *et al* 2001, Mishra *et al* 2001, 2002, 2005, 2006a, 2006b, Ouillon *et al* 2002, Meyer *et al* 2002, Yamanaka *et al* 2002, Gallardo *et al* 2003, Harrison *et al* 2003, Ranson *et al* 2005, Howard *et al* 2005, Woodward *et al* 2006). In addition to their intrinsic scientific interest as materials with coupled phase transitions, CST perovskites are used in geosciences as analogues to represent the likely behaviour of silicate perovskites in the earth's mantle (Sasaki *et al* 1987, Liu and Liebermann 1993, Guyot *et al* 1993, Gillet *et al* 1993, Redfern 1996, Yamanaka *et al* 2002). The CST solid solution displays substantial anomalies in elastic properties associated with the phase transitions (Harrison *et al* 2003, Carpenter 2007a, 2007b, Carpenter *et al* 2007), for example. $CaTiO_3$ has also been proposed as a suitable host material for the containment of selected elements present in radioactive waste (Ringwood *et al* 1988).

Structural evolution of Ca-rich members of the CST solid solution is dominated by the same coupled tilting transitions as are found in CST0. For compositions in the range ~$Ca_{0.6}Sr_{0.4}TiO_3$–$Ca_{0.4}Sr_{0.6}TiO_3$ (CST40–CST60), however, the overtly orthorhombic lattice geometry of the lowest symmetry structure becomes nearly cubic. This change in geometry led to the suggestion that the space group for intermediate members of the solid solution at room temperature is *Cmcm* (Ball *et al* 1998). More recent investigations have shown that the correct space group symmetry is $Pnma$ from CST0 to ~CST59 (Ranjan *et al* 1999, 2001, Howard *et al* 2001, Mishra *et al* 2006b) and $Pbcm$ between ~CST60 and ~CST64 (Ranjan *et al* 2001, Mishra *et al* 2006b). The sequence of structural states for compositions between ~CST65 and ~CST94 has also been controversial. Gränicher and Jakits (1954), McQuarrie (1955) and Mitsui and Westphal (1961) described tetragonal lattice geometry for samples with compositions in this range at room temperature, and $I4/mcm$ symmetry has since been reported in a number of subsequent studies (Ball *et al* 1998, Qin *et al* 2000, 2002, Yamanaka *et al* 2002, Howard *et al* 2005). On the other hand, Ranjan and Pandey (1999, 2001b), Ranjan *et al* (2000), Mishra *et al* (2001) and Ouillon *et al* (2002) argued that the $I4/mcm$ structure is stable over only a small temperature interval before giving way to an orthorhombic structure with $Pnma$ or $Imma$ symmetry. In more recent papers, Ranson *et al* (2005) and Mishra *et al* (2005, 2006a) have shown the transition from the cubic phase as being directly to a structure with $Imma$ symmetry. Woodward *et al* (2006) subsequently proposed that samples with compositions CST50 and CST80 actually have monoclinic symmetry at room temperature. Finally, a transition involving the development of ferroelectric domains at low temperatures in the most Sr-rich compositions has also attracted a great deal of attention, starting with the work of Mitsui and Westphal (1961) and Bednorz and Müller (1984). In CST99.3 the transition occurs at ~18 K and is marked by anomalies in dielectric properties, optical birefringence and the temperature dependence of selected bands in Raman spectra (Bianchi *et al* 1994a, 1994b, 1995, Kleemann *et al* 1995, 1997). Increasing Ca content causes the transition temperature to rise to ~35 K, but the anomaly in dielectric properties becomes increasingly smeared out (Bednorz and Müller 1984).

The primary objective of the present study was to make use of the high resolution capabilities of neutron powder diffraction and synchrotron x-ray powder diffraction to examine structural relationships in detail as a function of temperature for critical compositions across the CST solid solution. Following the approach of Carpenter *et al* (2001, 2005), high precision lattice parameters have been converted to symmetry-adapted strains in order to follow the

evolution of different order parameter components for the coupled phase transitions. These, in turn, have been compared with the evolution of octahedral tilt angles extracted from the powder diffraction data by Rietveld structure refinement. In combination with previous data from the literature, the results define an internally consistent topology for a temperature–composition phase diagram relating to samples prepared at high temperatures and furnace cooled. The composition and temperature dependence of each of the known phase transitions also provides insights into the relationships between the different structure types that are observed. Details of the procedures used for sample preparation and data collection are given in section 2. Section 3 includes technical information about the structure refinements and the new lattice parameter data obtained from them. Our proposed phase diagram is then introduced in section 4. Section 5 contains formal descriptions of each structure type and phase transition in terms of spontaneous strains, order parameter components and octahedral tilt angles. Section 6 is a brief comparison of strain and octahedral tilt properties as a function of composition across the solid solution at room temperature. Finally, separate aspects of the observed behaviour of CST perovskites are drawn together in a more general discussion in section 7.

2. Experimental methods

2.1. Sample preparation

The samples used in this work were all prepared by the alkoxide/nitrate route (Ringwood *et al* 1988). Samples CST20, CST25 and CST70 were prepared previously for other studies, while the remaining samples, CST56, CST58, CST59, CST63, CST85, CST87, CST90 and CST95, were produced for the present study. The alkoxide/nitrate method involved the mixing of correct molar quantities of Ti isopropoxide with aqueous solutions of Sr and Ca nitrates, while continuously stirring. After thorough mixing and stir drying, the materials were calcined in air at 750 °C for 1 h, followed by wet milling for 16 h using zirconia balls. Each slurry was dried at 110 °C overnight, then the dried clumps were ground in a mortar and pestle into fine powder. The powders were pressed into 10 g pellets, and finally sintered in air under slightly different conditions: at 1550 °C for 85 h for CST25 (Ball *et al* 1998), 1500 °C for 6 h for CST20, and 1550 °C for 96 h for the remaining (majority of the) samples. The sample compositions were checked using a JEOL 6400 scanning electron microscope fitted with an energy dispersive spectrometer. The SEM analyses showed all samples to be homogeneous solid solutions, with trace amounts of rutile in some of them. Samples were ground to powder prior to the diffraction measurements.

2.2. Neutron diffraction

Neutron diffraction data were recorded using the high-resolution powder diffractometer, HRPD, at the ISIS neutron facility, Rutherford Appleton Laboratories, UK (Ibberson *et al* 1992). Measurements were made at temperatures ranging in total from 4.2 to 1473 K, the actual ranges being different for different compositions. This necessitated the use of a cryostat, capable of measurement from 4.2 to 450 K, and furnaces to 1273 or 1473 K. Measurements on CST20 and CST25 were made in the furnaces, whereas for CST58, CST59, CST85, CST87, CST90 and CST95 only the cryostat was used. For CST56 and CST63 measurements were made in both cryostat and furnace, and in each case an attempt was made to ensure overlap of the measurement temperatures.

For measurements in the cryostat, the powdered sample was lightly packed into an aluminium can of slab geometry, 20 by 20 mm in cross section and 15 mm thick, with thin

neutron-transparent windows front and back. Heat was supplied to the sample through a 100 W cartridge heater inserted in the side wall of the sample holder. Temperature was monitored using a Rh/Fe sensor located in the opposite wall. A neutron-absorbing gadolinium mask was attached to the front of the can facing the incident beam (and back-scattering detectors) so as to prevent contaminant Bragg peaks arising from either the body of the sample can, including sensor and heater, or the stainless steel frames supporting the vanadium windows. The assembly was attached to a centre-stick and mounted in an AS Scientific, 50 mm diameter, 'Orange' helium cryostat, located at the 1 m position of the diffractometer. The exchange gas was helium at 30 mbar. For data collection at high temperatures each sample was loaded into a 11 mm diameter vanadium sample can, which was mounted in an RAL vacuum furnace with vanadium heating elements. Thermometry was based on type-K thermocouples positioned in contact with the sample can at about 20 mm above the beam centre. The sample temperature, in the cryostat or furnace, was controlled to ± 0.2 K.

Diffraction patterns were recorded over the time-of-flight range 30–130 ms, corresponding to a d-spacing range 0.6–2.6 Å, or 0.9–3.7 Å, for patterns collected in the back-scattering and 90 degree detector banks respectively. Some recent examples of diffraction patterns collected on HRPD are illustrated for a variety of perovskites in Howard *et al* (2000), Hayward *et al* (2005) and Kennedy *et al* (2006). Measurements on CST20 and CST25 predated the upgrading of the HRPD 90 degree banks, so for these two compositions only back-scattering patterns were obtained. The patterns were normalized to the incident beam spectrum as recorded in the upstream monitor, and corrected for detector efficiency according to prior calibration with a vanadium scan. The temperature intervals were typically 10 K, but varied from 2 to 50 K depending on the perceived proximity of phase transitions or other features of interest. In order to allow for thermal equilibration of the sample, data collection was delayed for a period of at least 5 min (depending on the size of the temperature step) after the set point was reached. Most patterns were then recorded to a total incident proton beam of about 10 μA h, corresponding to about 20 min of data collection. This is sufficient to give well constrained determinations of lattice parameters, and reasonable estimates of internal parameters. Longer counting times in the range 35 to 100 μA h were used in order to obtain better estimates of internal coordinates in a number of cases.

2.3. Synchrotron x-ray diffraction

This paper incorporates results from an x-ray synchrotron study, at SPring-8, Hyogo, Japan, of CST70 at room temperature and above. Details of the sample and experimental procedure, as well as the original data, are given by Howard *et al* (2005). Additional diffraction patterns were subsequently collected in the temperature range 100–300 K, and results from these are presented here. Experimental details for the low temperature measurements are the same as for the measurements above room temperature, except that the capillaries used were plain glass and the heated nitrogen gas flow became a flow of cooled nitrogen gas.

3. Data analysis

3.1. Identification of phases

Different phases were identified by close inspection of the diffraction patterns, paying particular attention to peak splittings and the presence or absence of various superlattice peaks. First the peaks were indexed on the basic perovskite cell: the main peaks (even if they show splitting) have integral indices, whereas any superlattice peaks show fractional indexing. Peak splitting

was used to help establish the symmetry of the variant under study. For example, tetragonal symmetry is expected to lead to doublet splitting of the $h00$ type reflections, while leaving the hhh type reflections as singlets. The reverse occurrence would be indicative of rhombohedral splitting. More complex patterns of splitting indicate orthorhombic or monoclinic symmetry. The splitting of $h00$ type reflections has been particularly important in distinguishing the tetragonal structure in $I4/mcm$ from a proposed, pseudo-tetragonal structure in $Imma$. It is shown here (section 5.2) and elsewhere (Howard *et al* 2005) that in the latter structure the splitting would be about half the size and the intensities in the doublet reversed. Superlattice peaks were marked according to the $\boldsymbol{k}$ value of the reciprocal lattice point associated with the relevant distortion. The distortions of main interest here are the usual octahedral tilting distortions, the in-phase tilting being associated with irreducible representation (irrep) M_3^+ ($\boldsymbol{k} = 1/2, 1/2, 0$) and the out-of-phase tilting being associated with R_4^+ ($\boldsymbol{k} = 1/2, 1/2, 1/2$). A somewhat unusual tilting pattern, wherein two successive layers of octahedra tilt in one sense and the next two layers in the opposite sense, is associated with irrep T_4 at the $\alpha = 1/4$ point on the T line ($\boldsymbol{k} = 1/2, 1/2, \alpha$). Although this is not a point of special symmetry, it is referred to below for the sake of brevity as the 'T point'. This tilting appears to be a primary distortion in the $Pbcm$ structure first reported by Ranjan *et al* (2000) for compositions around CST60 and then confirmed in a number of subsequent studies (Ranjan *et al* 2001, Mishra *et al* 2002, 2006b, Howard *et al* 2006). Distortions at the M point ($\boldsymbol{k} = 1/2, 1/2, 0$), R point ($\boldsymbol{k} = 1/2, 1/2, 1/2$) and T point ($\boldsymbol{k} = 1/2, 1/2, 1/4$) give rise to superlattice peaks indexing with one integral two half-integral indices, three half-integral indices, and two half-integral one quarter-integral indices, respectively. In addition, the coupling of distortions at different points of reciprocal space can give rise to distortions that produce intensities at the sum or difference points. Specifically, the simultaneous presence of R and M point tilting can produce weaker intensity at the X points ($\boldsymbol{k} = 0, 0, 1/2$; two integral, one half-integral indices), whereas the simultaneous presence of R and T point tilting can produce weak intensities at the Δ point ($\boldsymbol{k} = 0, 0, 1/4$; two integral, one quarter-integral indices) and at the M point as well. General procedures for identifying the phases have been explained in greater detail elsewhere (Howard and Stokes 2005), and their specific application to this and very similar systems can also be found in the literature (Howard *et al* 2000, 2001, 2004, 2005, 2006).

All the diffraction patterns were consistent with structures having $Pm\bar{3}m$, $I4/mcm$, $Pnma$ or $Pbcm$ symmetry. Two-phase mixtures were found at the necessarily discontinuous transitions from $Pnma$ or $Pbcm$ to $I4/mcm$, or from $Pbcm$ to $Pnma$. It is important to note that $h00$ peaks showed different splitting in $I4/mcm$ as compared with either $Pnma$ or $Pbcm$. The corresponding two-phase regions were recognized from the presence of M or T point superlattice peaks together with evidence of superposition of these two different splittings in the pattern. There was a narrow two-phase region between the structures in $Pnma$ and $Pbcm$, as recognized by changing relative intensities of peaks at the T and M points. T point reflections correspond to a primary distortion in $Pbcm$; M point reflections correspond to a primary distortion in $Pnma$ but are weaker in $Pbcm$, where they are due to the concerted action of R and T point distortions.

3.2. Rietveld refinement

Structure types were confirmed and lattice parameters plus atomic coordinates determined using the Rietveld method as implemented in the GSAS computer program (Rietveld 1969, Larson and Von Dreele 2000, Toby 2001). Starting structures were taken from Kennedy *et al* (1999) for $Pm\bar{3}m$ and $I4/mcm$ structures, from Howard *et al* (2001) for the $Pnma$ structure, and from Howard *et al* (2006) for the $Pbcm$ structure. Patterns from the back-scattering and,

where available, 90 degree banks were fitted simultaneously. The diffractometer constant for the 90 degree bank was released to ensure that lattice parameters were determined by the higher resolution back-scattering bank in each case. Peak shape was modelled as the convolution of two back to back exponentials with a pseudo-Voigt function in which two or, for the 90 degree bank, three peak width parameters were varied, and the background by shifted Chebyshev polynomials. Internal coordinates were refined along with displacement parameters. Oxygen displacement parameters were taken to be anisotropic for tetragonal and cubic structures, but isotropic for orthorhombic structures. In each case the proportion of calcium and strontium atoms was fixed on the basis of the bulk chemical composition and they were taken to be distributed randomly on their shared site, with their displacement parameters constrained to be equal. The fits in single-phase regions were quite satisfactory in every case, with weighted profile *R*-factors, R_{wp}, in the range ∼5–10% and chi squared values from ∼7 down to 1.03 depending mostly on the counting time.

Rietveld analysis was also useful in confirming the two-phase regions associated with the various first order transitions. These regions became evident by degradation of the fits when pure phases were assumed. In a few cases, for CST63 for example, refinements assuming two-phase mixtures were successfully completed. In other cases, for CST20 for example, the anomalous behaviour of lattice parameters obtained from the Rietveld refinements can be taken as an indication of the presence of the second phase.

3.3. Lattice parameters

Lattice parameter data are given in reduced form in figure 1, i.e. as a for the cubic structure, $a/\sqrt{2}$ and $c/2$ for the $I4/mcm$ structure, $a/\sqrt{2}$, $b/2$, $c/\sqrt{2}$ for the $Pnma$ structure and $a/\sqrt{2}$, $b/\sqrt{2}$, $c/4$ for the $Pbcm$ structure. Results for CST58 and CST87 are not shown since measurements from these samples covered only a very limited range of temperatures. Nominal statistical errors indicated by the GSAS program were mostly of the order of one part in 10^5, much smaller than the size of symbols used in the plots. The scatter of points gives a more realistic indication of error, but again suggests that uncertainties are probably less than the size of the symbols.

Mishra *et al* (2006a) reported lattice parameter data for samples with compositions CST57 and CST60 (their figures 5 and 3). Aside from the fact that they used $Imma$ symmetry with tetragonal lattice geometry for CST60, their data are in close agreement with the variations reported here for CST56 and CST63, respectively.

3.4. Octahedral tilt angles

Octahedral tilt angles were derived from refined oxygen coordinates as follows.

- $I4/mcm$: the Ti atom is at the origin, and the tilt angle is determined by location of the 'equatorial' oxygen O2, at $1/4 + u$, $3/4 + u$, 0 (Kennedy *et al* 1999). This is out-of-phase R point tilting around an axis along the [001] direction of the cubic parent, and the angle is given by $\tan\phi_R = 4u$.
- $Pnma$: the Ti atom remains at the origin. This structure shows R and M point tilting around axes along cubic [011] and [100] respectively. Both tilt angles can be estimated from the coordinates of the equatorial oxygen, labelled O2, using $\tan\phi_R = -4\sqrt{2}y(\mathrm{O2})$, $\tan\phi_M = 2(x(\mathrm{O2}) - z(\mathrm{O2}))$. Another estimate for the R point tilting can be obtained from the 'apical' oxygen, O1, using $\tan\phi_R = 2\sqrt{2}z(\mathrm{O1})$. The two different estimates of ϕ_R are equal under the condition $z(\mathrm{O1}) = -2y(\mathrm{O2})$, as would be the case for rigid octahedra. The space group symmetry does not require that the octahedra are rigid, but in practice this

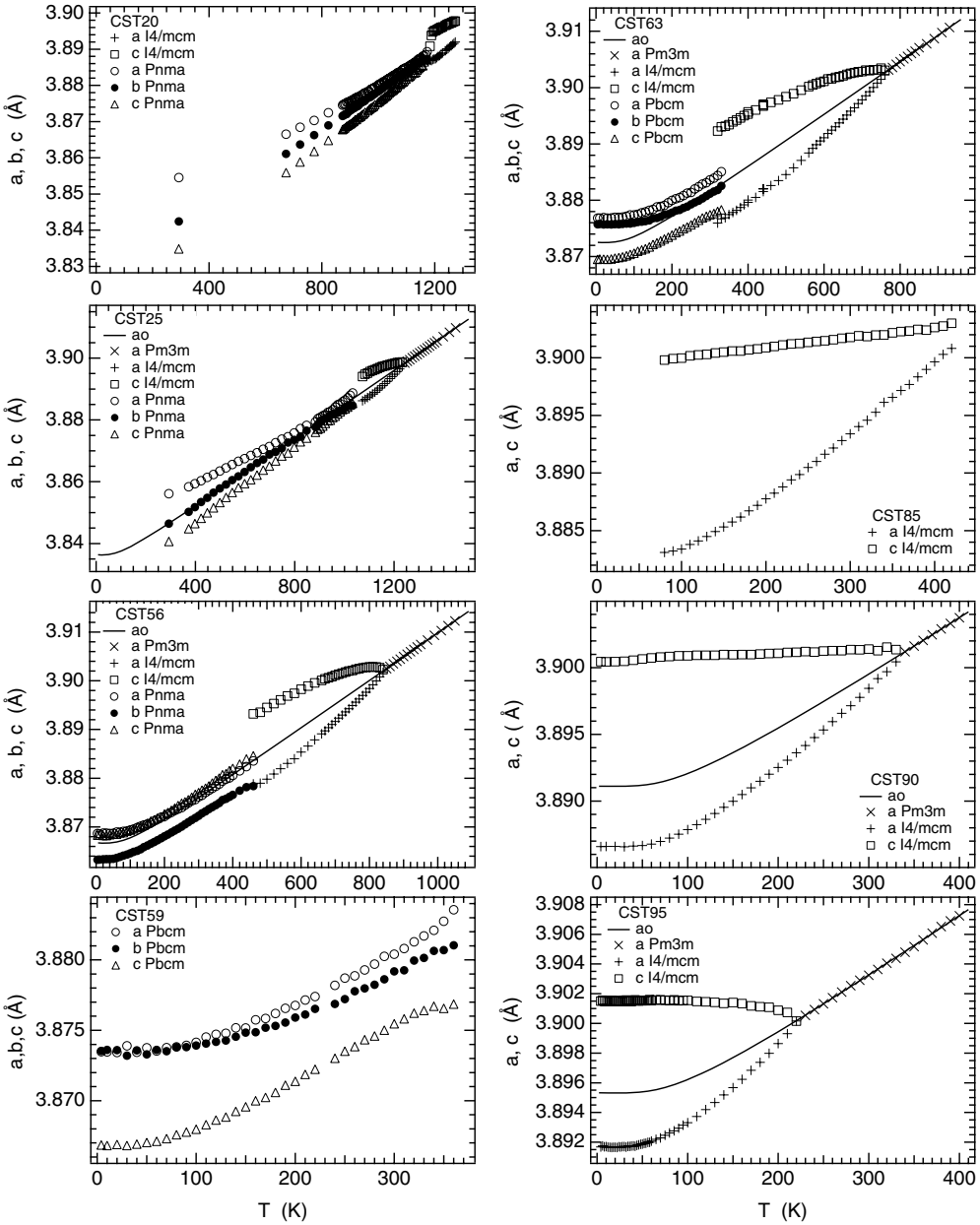

Figure 1. Reduced lattice parameters as a function of temperature at different compositions across the CST solid solution. Solid lines are fits of (29) to the data for cubic structures at high temperatures, with Θ_s fixed at 128.1 K.

condition is reasonably well satisfied. It is often convenient to report the average. More detail can be found in the paper by Kennedy *et al* (1999), though these authors used the alternative *Pbnm* setting of the space group.

- *Pbcm*: in this case the Ti atom is no longer at the origin, but is located close to 1/4, 1/4, 1/8. The structure shows R and T point tilting around axes along cubic [011]

and [100] respectively. From the positions of the apical oxygens, O1 and O2 (labelling as per Mishra *et al* 2006b, Howard *et al* 2006), an estimate of the tilt angle associated with the R point can be obtained using $\tan\phi_R = \sqrt{2}(x(O1) - x(O2))$. Based on the positions of the equatorial oxygens, O3 and O4, another estimate of this angle can be obtained, using $\tan\phi_R = 4\sqrt{2}(z(O3) - z(O4))$; the two estimates are consistent provided $x(O1) - x(O2) = 4(z(O3) - z(O4))$, which we find to be approximately the case. The estimate of the tilt angle associated with the T point is based on the positions of the equatorial oxygens, using $\tan\phi_T = x(O3) + y(O3) - x(O4) - y(O4)$.

Values of tilt angles are much less well constrained than values of the lattice parameters since the refined oxygen coordinates depend very much on fits to relatively weak superlattice peaks. The fitting is sensitive, firstly, to the background as modelled in the Rietveld program, and, secondly, to the widths of these weak reflections, which sometimes do not appear to correspond to the widths of the stronger peaks. Determination of more tightly constrained tilt angles requires primary diffraction patterns collected for longer times than were used in this study.

4. Phase diagram

Figure 2 shows a phase diagram for CST perovskites based on data from the literature and from the new powder diffraction experiments presented here. Transition temperatures given by Qin *et al* (2000) for transitions above room temperature were determined by differential scanning calorimetry using samples with compositions in the range CST0–CST80. Transition temperatures given by Harrison *et al* (2003) for samples with compositions in the range CST50–CST90 were based on observations of anomalies in bulk elastic properties detected by dynamical mechanical analysis. These two sets of data combine to give a well constrained trend for the cubic ↔ tetragonal transition that is in close agreement with data from diffraction experiments (Ranjan and Pandey (2001b) for CST70–CST88, Ali and Yashima (2005) for CST0, Howard *et al* (2005) for CST70, Mishra *et al* (2006a) for CST57 and CST60, this study for CST20–CST95). The trend is also consistent with the extension to low temperatures based on data from optical birefringence measurements (Bianchi 1996, in Lemanov 1997), calorimetry (Gallardo *et al* 2003) and diffraction (Mishra *et al* 2005, this study). Only the transition temperature of Mishra *et al* (2005) for CST94 appears to be anomalous in falling above the overall trend and ∼60 K above the value given for a sample with the same nominal composition by Lemanov (1997) after Bianchi (1996). The transition temperature of 106 K for $SrTiO_3$ has been taken from Hayward and Salje (1999). Published data for the transition temperatures of $CaTiO_3$ vary widely, as reviewed by Ali and Yashima (2005). The values of the latter authors have been used here (1634 ± 13, 1498 ± 25 K).

The solid curve in figure 2 is a fit to the data using the function

$$T_{cx} = \frac{\Theta_s}{\coth^{-1}\left(\coth\left(\frac{\Theta_s}{T_c}\right) - kx\right)}, \tag{1}$$

where T_{cx} is the cubic ↔ tetragonal transition temperature at different compositions, x is the proportion of $SrTiO_3$ component in mol%, and $\Theta_s = 274$ K, $T_c = 1621$, $k = 0.05$ (Carpenter 2007b). This represents the behaviour of a transition in which the non-linear evolution as $T_c \rightarrow 0$ K is determined by a saturation temperature, Θ_s, (Hayward and Salje 1998). While not necessarily providing the correct physical explanation of the non-linearity, it provides a convenient description of the data.

The first order $I4/mcm \leftrightarrow Pnma$ transition is marked by a temperature interval of ∼20–30 K over which the tetragonal and orthorhombic structures coexist (Mishra *et al* 2006a, this

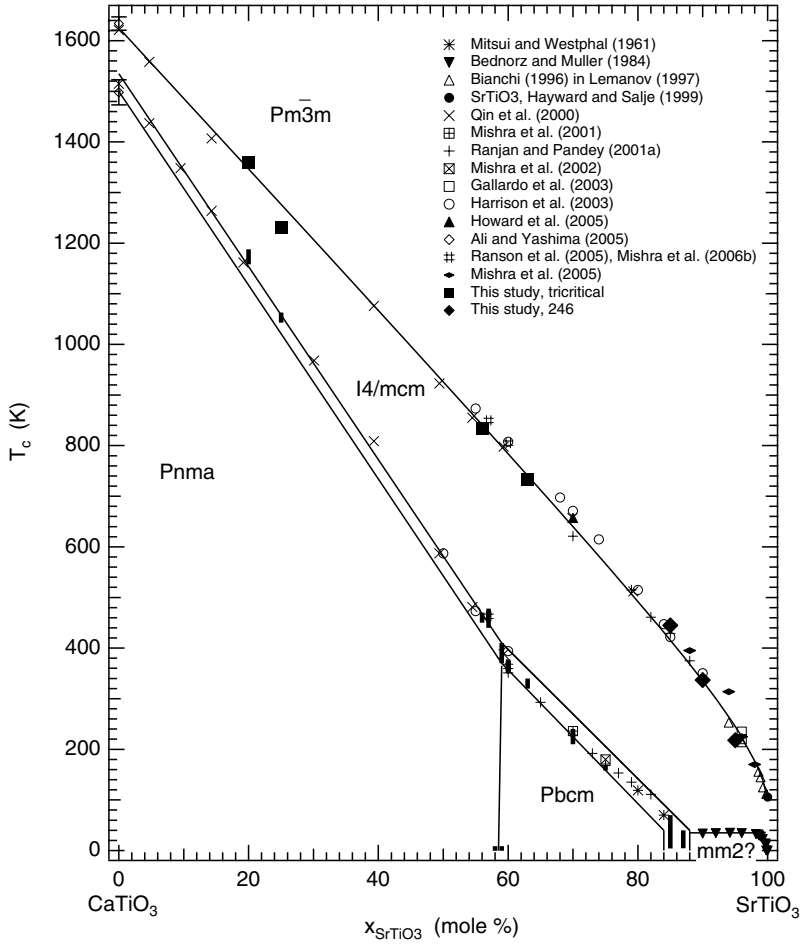

Figure 2. Phase diagram for (Ca, Sr)TiO_3 perovskites based on transition temperatures obtained from *in situ* studies of samples with different compositions across the solid solution. Vertical bars signify the composition limits of two coexisting structures: CST20, CST25, CST56, CST59, CST63, CST70, CST85, CST87 from this study; CST57, CST60 from Mishra *et al* (2006a); CST70, CST75 from Ranjan and Pandey (2001a). Two-phase regions separating $I4/mcm$ fields from $Pnma$ and $Pbcm$ fields are shown schematically as being bounded by parallel lines. The steep slope of the $Pnma/Pbcm$ boundary is constrained by the observations that CST58 has the $Pnma$ structure and CST59 the $Pbcm$ structure at 4.2 K. The curve representing T_c for the $Pm\bar{3}m \leftrightarrow I4/mcm$ transition is a fit of (1) (Carpenter 2007b).

study). There is reasonable agreement between transition temperatures estimated on the basis of a sharp anomaly in heat capacity (Qin *et al* 2000), anomalies in bulk elastic properties (Harrison *et al* 2003) and changes in powder diffraction patterns (Ali and Yashima 2005, Mishra *et al* 2006a, this study). The equivalent transition in Sr-rich compositions is marked by a similar two-phase field of coexisting structures ($Pnma$ or $Imma + Pbcm$ according to Ranjan *et al* 2000, Ranjan and Pandey 2001b, Mishra *et al* 2006a, $I4/mcm + Pbcm$ in this study). Again there is good agreement between transition temperatures extracted from diffraction results (Ranjan and Pandey 2001b, Mishra *et al* 2002, 2006a, this study) and values based on observations of an anomaly in dielectric properties (Mitsui and Westphal 1961, Ranjan *et al* 2000, Ranjan and

Pandey 2001a, Mishra *et al* 2002, 2006a). Each of the two-phase fields is shown arbitrarily as being bounded by parallel lines in figure 2. Under equilibrium conditions, both would be defined by two-phase loops of coexisting tetragonal and orthorhombic structures with different compositions. Although the boundary between $Pnma$ and $Pbcm$ fields should likewise involve coexisting structures, the $Pnma \leftrightarrow Pbcm$ transition in CST59 appears to occur between 340 and 350 K with a rather narrower range of two-phase coexistence. A steep boundary between the stability fields of these two structures is defined by the observation that CST58 and CST59 have diffraction patterns consistent with $Pnma$ and $Pbcm$ symmetry, respectively, at 4.2 K.

Data for the transition with $T_c \leqslant \sim 35$ K in samples containing more than ~90% $SrTiO_3$ have been reproduced from Bednorz and Müller (1984). The point group of crystals with composition CST99.3 is $mm2$ below the transition point (Bianchi *et al* 1994b, 1995, Kleemann *et al* 1997), but the present authors are not aware of any symmetry determination for other compositions. Accordingly, the low temperature field has been labelled as '$mm2$?' in figure 2. Ranjan *et al* (2000), Ranjan and Pandey (2001b), Ouillon *et al* (2002) and Ranson *et al* (2005) show the low temperature field as being for a relaxor ferroelectric for most of its composition range. There is only the slightest evidence of a change in lattice geometry at the transition point in the high precision lattice parameter data presented here for CST90 and CST95 (figure 1). The topology of the phase boundary between this nominally orthorhombic structure and the $Pbcm$ structure is not known. From the extent of two-phase fields ($I4/mcm + Pbcm$) in samples with compositions CST85 and CST87, it is assumed to be a two-phase loop which is wider than 2 mol% $SrTiO_3$.

This phase diagram preserves elements of the phase diagrams originally proposed by Mitsui and Westphal (1961) for low temperatures and Qin *et al* (2000) for high temperatures. It differs from phase diagrams shown by Ranjan *et al* (2000), Ranjan and Pandey (2001b), Ouillon *et al* (2002) and Ranson *et al* (2005) in having a broad stability field for the $I4/mcm$ structure that extends across the entire solid solution between the stability fields of the high temperature, cubic structure and the low temperature orthorhombic structures. As discussed in more detail below, we have not found evidence for a structure with $Imma$ symmetry. Ranjan *et al* (2000), Ranson *et al* (2005) and Mishra *et al* (2006a) reported additional anomalies in dielectric properties and Raman spectra which might indicate a further phase transition below ~150 K for samples with compositions CST60 and CST70. There is no indication of these in diffraction data for CST60 (Mishra *et al* 2006a) or CST63 (this study), however. Our data for CST56 (figure 1) do not show the break in slope at ~100 K reported by Mishra *et al* (2006a) for CST57.

5. Structural relationships: octahedral tilting and spontaneous strain

5.1. Strain/order parameter coupling relationships

Octahedral tilting transitions associated with the M and R points of the reciprocal lattice of a parent perovskite structure with $Pm\bar{3}m$ symmetry can be described using a Landau free energy expansion of the form

$$\begin{aligned} G = {} & \frac{1}{2}a_1\Theta_{s1}\left(\coth\left(\frac{\Theta_{s1}}{T}\right) - \coth\left(\frac{\Theta_{s1}}{T_{c1}}\right)\right)\left(q_1^2+q_2^2+q_3^2\right) + \frac{1}{2}a_2\Theta_{s2}\left(\coth\left(\frac{\Theta_{s2}}{T}\right)\right. \\ & \left. - \coth\left(\frac{\Theta_{s2}}{T_{c2}}\right)\right)\left(q_4^2+q_5^2+q_6^2\right) + \frac{1}{4}b_1\left(q_1^2+q_2^2+q_3^2\right)^2 + \frac{1}{4}b_1'\left(q_1^4+q_2^4+q_3^4\right) \\ & + \tfrac{1}{4}b_2\left(q_4^2+q_5^2+q_6^2\right)^2 + \tfrac{1}{4}b_2'\left(q_4^4+q_5^4+q_6^4\right) + \tfrac{1}{6}c_1\left(q_1^2+q_2^2+q_3^2\right)^3 \\ & + \tfrac{1}{6}c_1'\left(q_1q_2q_3\right)^2 + \tfrac{1}{6}c_1''\left(q_1^2+q_2^2+q_3^2\right)\left(q_1^4+q_2^4+q_3^4\right) \end{aligned}$$

$$
\begin{aligned}
&+ \tfrac{1}{6}c_2\left(q_4^2+q_5^2+q_6^2\right)^3 + \tfrac{1}{6}c_2'\left(q_4q_5q_6\right)^2 + \tfrac{1}{6}c_2''\left(q_4^2+q_5^2+q_6^2\right)\left(q_4^4+q_5^4+q_6^4\right)\\
&+ \lambda_{\mathrm{q}}\left(q_1^2+q_2^2+q_3^2\right)\left(q_4^2+q_5^2+q_6^2\right) + \lambda_{\mathrm{q}}'\left(q_1^2q_4^2+q_2^2q_5^2+q_3^2q_6^2\right)\\
&+ \lambda_1 e_{\mathrm{a}}\left(q_1^2+q_2^2+q_3^2\right) + \lambda_2 e_{\mathrm{a}}\left(q_4^2+q_5^2+q_6^2\right)\\
&+ \lambda_3\left[\sqrt{3}e_{\mathrm{o}}\left(q_2^2-q_3^2\right) + e_{\mathrm{t}}\left(2q_1^2-q_2^2-q_3^2\right)\right]\\
&+ \lambda_4\left[\sqrt{3}e_{\mathrm{o}}\left(q_5^2-q_6^2\right) + e_{\mathrm{t}}\left(2q_4^2-q_5^2-q_6^2\right)\right] + \lambda_5\left(e_4q_4q_6+e_5q_4q_5+e_6q_5q_6\right)\\
&+ \lambda_6\left(q_1^2+q_2^2+q_3^2\right)\left(e_4^2+e_5^2+e_6^2\right) + \lambda_7\left(q_1^2e_6^2+q_2^2e_4^2+q_3^2e_5^2\right)\\
&+ \tfrac{1}{4}\left(C_{11}^{\mathrm{o}}-C_{12}^{\mathrm{o}}\right)\left(e_{\mathrm{o}}^2+e_{\mathrm{t}}^2\right) + \tfrac{1}{6}\left(C_{11}^{\mathrm{o}}+2C_{12}^{\mathrm{o}}\right)e_{\mathrm{a}}^2 + \tfrac{1}{2}C_{44}^{\mathrm{o}}\left(e_4^2+e_5^2+e_6^2\right). \qquad (2)
\end{aligned}
$$

Here q_1–q_3 are order parameter components for the M_3^+ instability, q_4–q_6 are order parameter components for the R_4^+ instability, a_1, a_2, b_1, etc, are normal Landau coefficients, $T_{\mathrm{c}1}$, $T_{\mathrm{c}2}$ are critical temperatures, $\Theta_{\mathrm{s}1}$ and $\Theta_{\mathrm{s}2}$ are saturation temperatures, λ_1, λ_3, etc, are coupling coefficients, C_{11}^{o}, C_{12}^{o}, C_{44}^{o} are elastic constants of the cubic structure and e_4, e_5, e_6 are shear strain components. The symmetry-adapted strains e_{a}, e_{o} and e_{t} are combinations of the linear strain components, e_1, e_2, e_3, as

$$e_{\mathrm{a}} = (e_1+e_2+e_3) \qquad (3)$$

$$e_{\mathrm{o}} = (e_1-e_2) \qquad (4)$$

$$e_{\mathrm{t}} = \frac{1}{\sqrt{3}}(2e_3-e_1-e_2). \qquad (5)$$

Individual spontaneous strains are defined with respect to an orthogonal reference system where the parent cubic structure crystallographic axes x, y, z are parallel to reference axes X, Y, Z, respectively. This form of the Landau expansion was introduced by Carpenter *et al* (2001) and further developed by Carpenter (2007a), but is based upon expansions for phase transitions in perovskites which have been widely used (e.g. Laubereau and Zurek 1970, Slonczewski and Thomas 1970, Lüthi and Moran 1970, Rehwald 1970a, 1970b, Fossheim and Berre 1972, Okai and Yoshimoto 1975, Bulou *et al* 1992, Hayward and Salje 1999, Schranz *et al* 1999, Kityk *et al* 2000a, 2000b, Vanderbilt and Cohen 2001).

Following Howard and Stokes (1998) and Carpenter *et al* (2001), the geometrical description of tilting transitions in perovskites introduced by Glazer (1972, 1975) can be considered in terms of the order parameter components q_1–q_6. Specifically, octahedral tilt angles are expected to vary linearly with selected order parameter components, and each tilt system gives a macroscopic strain which is defined by setting the equilibrium conditions $\mathrm{d}G/\mathrm{d}e = 0$. The $I4/mcm$ structure has $q_4 \neq 0$, $q_1 = q_2 = q_3 = q_5 = q_6 = 0$, and the driving order parameter, q_4, is related to symmetry-adapted strains according to

$$e_{\mathrm{a}} = -\frac{\lambda_2 q_4^2}{\frac{1}{3}(C_{11}^{\mathrm{o}}+2C_{12}^{\mathrm{o}})} \qquad (6)$$

$$e_{\mathrm{t}} = -\frac{2\lambda_4 q_4^2}{\frac{1}{2}(C_{11}^{\mathrm{o}}-C_{12}^{\mathrm{o}})} \qquad (7)$$

$$e_{\mathrm{o}} = e_4 = e_5 = e_6 = 0. \qquad (8)$$

For the $Pnma$ structure ($q_4 = q_6 \neq 0$, $q_2 \neq 0$, $q_1 = q_3 = q_5 = 0$), equivalent relationships are

$$e_{\mathrm{a}} = -\left[\frac{\lambda_1 q_2^2 + 2\lambda_2 q_4^2}{\frac{1}{3}(C_{11}^{\mathrm{o}}+2C_{12}^{\mathrm{o}})}\right] \qquad (9)$$

$$e_{\mathrm{t}} = -\left[\frac{-\lambda_3 q_2^2 + \lambda_4 q_4^2}{\frac{1}{2}(C_{11}^{\mathrm{o}} - C_{12}^{\mathrm{o}})}\right] \tag{10}$$

$$e_{\mathrm{o}} = -\left[\frac{\lambda_3\sqrt{3} q_2^2 - \lambda_4\sqrt{3} q_4^2}{\frac{1}{2}(C_{11}^{\mathrm{o}} - C_{12}^{\mathrm{o}})}\right] \tag{11}$$

$$e_4 = -\frac{\lambda_5 q_4^2}{2(\lambda_6 + \lambda_7)q_2^2 + C_{44}^{\mathrm{o}}}. \tag{12}$$

These can be simplified by choosing the unique tetragonal axis to be parallel to the X-axis of the reference system, rather than the Z-axis, giving

$$e_{\mathrm{tx}} = -\left[\frac{2\lambda_3 q_2^2 - 2\lambda_4 q_4^2}{\frac{1}{2}(C_{11}^{\mathrm{o}} - C_{12}^{\mathrm{o}})}\right] \tag{13}$$

$$e_{\mathrm{ox}} = 0, \tag{14}$$

where

$$e_{\mathrm{tx}} = \frac{1}{\sqrt{3}}(2e_1 - e_2 - e_3) \tag{15}$$

$$e_{\mathrm{ox}} = (e_2 - e_3). \tag{16}$$

The $Pnma$ structure is a combination of $Imma$ and $P4/mbm$ tilts. If coupling between the M and R point tilts is weak, the variation of q_4 ($=q_6$) for the $Imma$ component is related to the same instability as q_4 for the $I4/mcm$ structure, but will be approximately half its magnitude, since

$$q_4^2 = \frac{-(b_2^* + b_2'^*) + \sqrt{(b_2^* + b_2'^*)^2 + 4a_2(c_2 + c_2'')\Theta_{\mathrm{s}2}\left(\coth(\frac{\Theta_{\mathrm{s}2}}{T_{\mathrm{c}2}}) - \coth(\frac{\Theta_{\mathrm{s}2}}{T})\right)}}{2\left(c_2 + c_2''\right)} \tag{17}$$

for $I4/mcm$ and

$$2q_4^2 = \frac{-(b_2^* + \frac{1}{2}b_2'^*) + \sqrt{(b_2^* + \frac{1}{2}b_2'^*)^2 + 4a_2(c_2 + \frac{1}{2}c_2'')\Theta_{\mathrm{s}2}\left(\coth(\frac{\Theta_{\mathrm{s}2}}{T_{\mathrm{c}2}}) - \coth(\frac{\Theta_{\mathrm{s}2}}{T})\right)}}{2\left(c_2 + \frac{1}{2}c_2''\right)} \tag{18}$$

for $Imma$. The renormalized fourth order coefficients are given by

$$b_2^* = b_2 - \frac{\lambda_5^2}{C_{44}^{\mathrm{o}}} - \frac{2\lambda_2^2}{\frac{1}{3}\left(C_{11}^{\mathrm{o}} + 2C_{12}^{\mathrm{o}}\right)} + \frac{4\lambda_4^2}{\frac{1}{2}\left(C_{11}^{\mathrm{o}} - C_{12}^{\mathrm{o}}\right)} \tag{19}$$

$$b_2'^* = b_2' + \frac{\lambda_5^2}{C_{44}^{\mathrm{o}}} - \frac{12\lambda_4^2}{\frac{1}{2}\left(C_{11}^{\mathrm{o}} - C_{12}^{\mathrm{o}}\right)}. \tag{20}$$

For the choice of non-zero order parameter components used here, the crystallographic axes of the $I4/mcm$ structure have a, b and c lattice parameters corresponding to [110], [$\bar{1}$10] and [002] of the parent cubic structure. The $Pnma$ (and $Imma$) structures have a, b and c corresponding to [011], [200], [01$\bar{1}$] (Howard and Stokes 1998, Carpenter *et al* 2001, 2005). In terms of measured lattice parameters, the linear strains are then given by

$$e_1 = e_2 = \frac{\left(\frac{a}{\sqrt{2}} - a_{\mathrm{o}}\right)}{a_{\mathrm{o}}} \tag{21}$$

$$e_3 = \frac{\left(\frac{c}{2} - a_{\mathrm{o}}\right)}{a_{\mathrm{o}}} \tag{22}$$

for the $I4/mcm$ structure, and

$$e_1 = \frac{\left(\frac{b}{2} - a_o\right)}{a_o} \tag{23}$$

$$e_2 + e_3 = \frac{\left(\frac{a}{\sqrt{2}} - a_o\right)}{a_o} + \frac{\left(\frac{c}{\sqrt{2}} - a_o\right)}{a_o} \tag{24}$$

$$|e_4| = \left| \frac{\left(\frac{a}{\sqrt{2}} - a_o\right)}{a_o} - \frac{\left(\frac{c}{\sqrt{2}} - a_o\right)}{a_o} \right| \tag{25}$$

for $Imma$ and $Pnma$ structures. The reference parameter, a_o, is, as usual, the lattice parameter of the cubic structure extrapolated to each temperature at which a, b and c of the low symmetry structures are measured.

The $Pbcm$ structure develops by coupling of a three component order parameter associated with the R point and a six component order parameter associated with T_4, a representation belonging to the T point which is located midway between the R and M points. Mishra *et al* (2006b) considered that this structure arose from a coupling of the tilting associated with the R point, irrep R_4^+, with an antiferroelectric pattern of Ti cation displacements corresponding to the symmetry of irrep Δ_5. From an examination of the structure, however (Howard *et al* 2006), it is clear that there is significant tilting corresponding to both R_4^+ and T_4, whereas there is only a small displacement of the Ti cation from the position it would occupy in the cubic aristotype. This leads us to suggest that the driving order parameters correspond to R_4^+ and T_4, with the antiferroelectric mode Δ_5 simply arising as a result of their combination. However, this antiferroelectric mode should be sufficient to account for the dielectric anomalies that have been reported at the transition to the $Pbcm$ phase (Ranjan and Pandey 2001a). A full symmetry analysis has not been completed for this structure but the group theory program ISOTROPY (Stokes and Hatch, Brigham Young University) has been used to check that strain/order parameter coupling terms for T_4 have the same form as for the M point. Only two of the six order parameter components are non-zero and these are equal in magnitude but opposite in sign. The orientation of interest for comparison with the $Pnma$ structure has **a**, **b**, **c** of the $Pbcm$ structure corresponding to $[01\bar{1}]$, [011], [400] of the parent cubic structure (Mishra *et al* 2006b). In this case the non-zero strains are given by

$$e_1 = \frac{\left(\frac{c}{4} - a_o\right)}{a_o} \tag{26}$$

$$e_2 + e_3 = \frac{\left(\frac{b}{\sqrt{2}} - a_o\right)}{a_o} + \frac{\left(\frac{a}{\sqrt{2}} - a_o\right)}{a_o} \tag{27}$$

$$|e_4| = \left| \frac{\left(\frac{b}{\sqrt{2}} - a_o\right)}{a_o} - \frac{\left(\frac{a}{\sqrt{2}} - a_o\right)}{a_o} \right|. \tag{28}$$

These strain relationships can be used to follow the evolution of order parameter components across a multi-dimensional order parameter space. When calculating spontaneous strains from the lattice parameter data, a_o was determined by fitting a function of the form

$$a_o = a_c + a_s \Theta_s \coth \frac{\Theta_s}{T} \tag{29}$$

to lattice parameters of the cubic phase at each composition (following Salje *et al* 1991, Meyer *et al* 2000, 2001, Sondergeld *et al* 2000, Carpenter *et al* 2003). This takes into account the

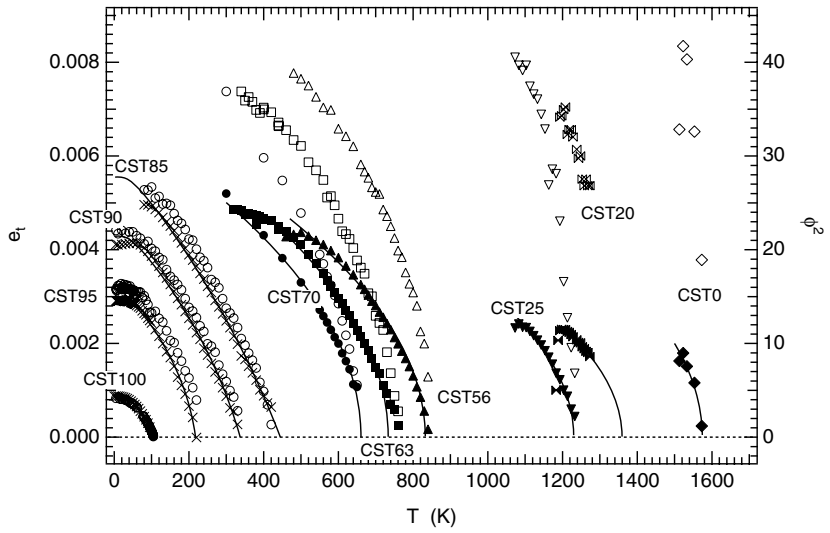

Figure 3. Variations of tetragonal shear strain, e_t (solid symbols or crosses, left axis), and the square of the octahedral tilt angle (open symbols, right axis, ϕ in units of degrees) for tetragonal CST perovskites. The left and right axes have been scaled so that there is an overlap of e_t (Carpenter 2007a) with ϕ^2 (Müller and Berlinger 1971, Müller *et al* 1991) for $SrTiO_3$. Values of e_t for $SrTiO_3$ were determined from lattice parameter variations of Okazaki and Kawaminami (1973) and Liu *et al* (1997). Data for $CaTiO_3$ (CST0) are from Kennedy *et al* (1999) with strains as calculated by Carpenter *et al* (2001). Note that a given tilt produces a larger strain as the $SrTiO_3$ content increases and that the tetragonal phase gives way to a low temperature structure at $\phi \approx 6°$–$7°$. Solid curves are fits to a function of the form $e_t \propto (T_c - T)^{0.5}$ (tricritical solution for $T \gg \Theta_{s2}$) for CST0–CST70, or a function of the form of (31) for CST85–CST100 (246 solution). $\Theta_{s2} = 60.8$, from the fit for $SrTiO_3$ given by Carpenter (2007a), was used for the 246 solution.

normal levelling off of volume as $T \rightarrow 0$ K through the saturation temperature, Θ_s (figure 1). A value of $\Theta_s = 128.1$ K has been taken from Carpenter (2007a) for $SrTiO_3$ and was assumed to remain constant across the solid solution.

5.2. The $Pm\bar{3}m \leftrightarrow I4/mcm$ transition

The order parameter, q_4, of the $I4/mcm$ structure is expected to scale linearly with the octahedral tilt angle, ϕ, and ϕ^2 is expected to vary linearly with the tetragonal strain, e_t. These parameters are shown as a function of temperature in figure 3 for each of the samples from which new experimental data have been obtained, together with data from Howard *et al* (2005) for CST70. They are scaled in such a way that data from the literature for e_t and ϕ^2 of $SrTiO_3$ overlap. The tilts and strains correlate semi-quantitatively in the expected manner but the amount of tetragonal strain for a given degree of octahedral tilt increases with increasing $SrTiO_3$ content. Thus the tetragonal $\leftrightarrow$ orthorhombic transition is reached at $\phi \approx 6.3°$ when the tetragonal strain is ~0.005 for CST70 and ~0.002 for CST0.

Uniform variations of ϕ and e_t are consistent with a field of stability of the $I4/mcm$ structure across the entire solid solution. Furthermore, individual data sets are consistent with the view that the transition to cubic symmetry is continuous. Linear variations of both ϕ^2 and e_t ($\propto q_4^2$) would imply second order character while the marked curvature that is observed is consistent with the transition having 246 or tricritical character at all compositions. If the first symmetry change for compositions in the range ~CST65–CST94 is $Pm\bar{3}m \leftrightarrow Imma$,

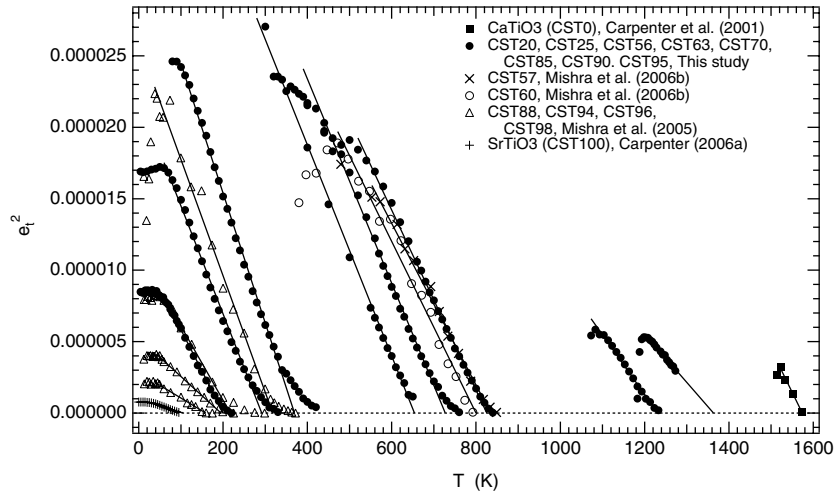

Figure 4. Variations with temperature of e_t^2 for the tetragonal structure at different compositions, including data from this study and from the literature. Data for CST0–CST70 are consistent with tricritical character, $e_t^2 \propto (T_c - T)$, with slopes that are generally quite similar. For CST85–CST100, there is a distinct tail above the extrapolation to zero strain of the linear fit, consistent with the transition evolving away from tricritical towards second order character. (Note that the average of a and b lattice parameters of the $Imma$ structure of CST60 given by Mishra *et al* (2006a) was used for the equivalent tetragonal parameters when calculating e_t for this composition.)

as proposed by Ranson *et al* (2005) and Mishra *et al* (2005, 2006a, 2006b), and is related to the same R point transition as the $I4/mcm$ structure, equations (7), (13), (17) and (18) (with $q_2 = 0$) imply that there should be significant differences in lattice parameter and strain evolution. Specifically, the tetragonal strain of the $Imma$ structure would be opposite in sign and approximately half the magnitude of the tetragonal strain for the $I4/mcm$ structure. Such a large difference in behaviour between different composition ranges would be obvious, and is not observed.

It has been proposed elsewhere that the cubic ↔ tetragonal transition in CST100 is intermediate between second order and tricritical in character (Salje *et al* 1998, Hayward and Salje 1999), but close to tricritical in CST0 (Carpenter *et al* 2001) and CST70 (Howard *et al* 2005, Carpenter 2007b, Carpenter *et al* 2007). Tricritical character would imply $(b_2^* + b_2'^*) = 0$, yielding a relationship of the form

$$e_t^2 = \frac{4\lambda_4^2 q_4^4}{\frac{1}{4}\left(C_{11}^o - C_{12}^o\right)^2} = \frac{4\lambda_4^2}{\frac{1}{4}\left(C_{11}^o - C_{12}^o\right)^2}\frac{a_2\Theta_{s2}}{\left(c_2 + c_2''\right)}\left(\coth\left(\frac{\Theta_{s2}}{T_{c2}}\right) - \coth\left(\frac{\Theta_{s2}}{T}\right)\right). \tag{30}$$

For $T \gg \Theta_{s2}$, this is equivalent to $e_t^2 \propto (T_c - T)$. Figure 4 shows e_t^2 from the new data plotted against temperature, together with strains calculated using lattice parameters given for a selection of other compositions by Mishra *et al* (2005, 2006a, 2006b). The latter are generally of lower resolution and do not permit the determination of reliable values for a_o, so the approximation $a_o = (a^2 c)^{1/3}$ was used when calculating e_t. The same approximation was also used for CST20, CST59 and CST85, because of the lack of data for the high temperature cubic phase. This does not introduce serious error since values of e_t are relatively insensitive to the choice of a_o.

As with the collected data in figure 3, the strain variations in figure 4 imply a more or less uniform pattern of structural evolution across the solid solution. For CST0–CST70, linear fits

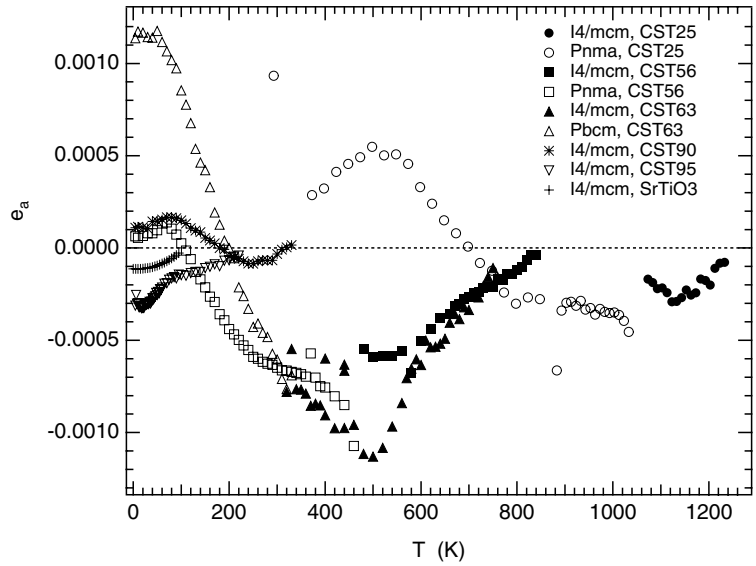

Figure 5. Variations of volume strain, e_a, extracted from those lattice parameter data which allowed reasonably tight constraints to be placed on the evolution of the cubic reference parameter, a_o, shown in figure 1. Absolute values of e_a are highly sensitive to the choice of a_o but the resulting data appear to be internally consistent. The negative volume strain at high temperatures has a marked curvature and tends to become positive at low temperatures. There is a small, discontinuous change in $|e_a|$ at the $I4/mcm \leftrightarrow Pnma$ transition, while e_a varies continuously through the $I4/mcm \leftrightarrow Pbcm$ transition. There are two values of e_a for CST25 which are clearly outliers, but no obvious experimental reason was found for excluding them.

provide a good description of the data over wide temperature intervals and give values of T_{c2} by extrapolation to $e_t^2 = 0$ which are in close agreement with transition temperatures determined by other means (figure 2). Gradients of the linear fits are also similar, suggesting that the various coefficients in (30) do not vary substantially with composition. For CST85–CST100, linear fits to the data generally describe the variations as $T \rightarrow T_c$ less well and also give values of T_c which fall below the values shown in figure 2. This is consistent with the view that the transition becomes 246 in character over this composition range. A function of the form

$$e_t \propto \frac{-B + \sqrt{B^2 + 4AC\Theta_{s2}\left(\coth(\frac{\Theta_{s2}}{T_{c2}}) - \coth(\frac{\Theta_{s2}}{T})\right)}}{2C}, \tag{31}$$

based on (17) and the assumption $e_t \propto q_4^2$, has therefore been fitted to the data in order to extract values of the transition temperatures. T_{c2} values obtained in this way have been added to figure 2 and show close agreement with previous determinations from the literature. As an aside, it is worth noting that in many of the data sets the temperature dependence of e_t becomes less steep as the stability fields of the $Pbcm$ or $Pnma$ structure are approached, implying that there may be precursor structural variations within the $I4/mcm$ structure.

Volume strains also display a fairly uniform pattern of evolution at different compositions (figure 5), though e_a does not scale linearly with e_t. Values of e_a are highly sensitive to the choice of a_o and only compositions for which reliable data for the cubic structure are available have been included in figure 5. The volume strain is small and negative in the stability field of the $I4/mcm$ structure but, after increasing in magnitude with increasing tilt angle, then starts to decrease. In the stability fields of the orthorhombic structures, it eventually becomes positive.

5.3. The $I4/mcm \leftrightarrow Pnma$ transition

Spontaneous strains and tilt angles for the *Pnma* structure at compositions CST0 (data of Kennedy *et al* 1999), CST20, CST25 and CST56 (this study) are shown in figure 6. Scaling of the axes was adjusted so that e_t and ϕ^2 of the $I4/mcm$ structure overlap. For each composition, the evolution of tilt angles is essentially the same. At the $I4/mcm \leftrightarrow Pnma$ transition point the R point tilt angle shows only a small discontinuity, implying that direct coupling between the M point and R point tilts is not particularly strong. The M point tilts develop discontinuously at the transition point and then increase smoothly with falling temperature. Values of the tetragonal strain, e_{tx}, for the *Pnma* structure immediately become small, as can be understood if the coupling coefficients λ_3 and λ_4 have the same sign. In this case contributions to e_{tx} from coupling with the R and M point tilts in (13) are opposite in sign. Values of the shear strain e_4 are expected to increase non-linearly with the R point tilt angle if the coupling coefficients λ_6 and λ_7 in (12) are significant. The increasingly steep variation of e_4 with falling temperature can be understood if these two coupling coefficients have negative sign. The evolution of e_4 is markedly different at CST56, in comparison with CST0, CST20 and CST25, formally reflecting the pseudocubic lattice geometry of intermediate members of the CST solid solution. Given that the tilt angles do not also drop at this composition, the implication is that the coupling coefficient λ_5 must be composition dependent, diminishing in magnitude with increasing $SrTiO_3$ content.

There appears to be a small negative volume strain associated with the $I4/mcm \leftrightarrow Pnma$ transition in samples with compositions CST25 and CST56 (figure 5). This implies that high pressures will stabilize the orthorhombic structure relative to the tetragonal structure. However, the magnitude of the volume strain diminishes with falling temperature, such that the cubic structure might be stabilized by high pressures with respect to both orthorhombic and tetragonal structures at the lowest temperatures.

5.4. The $I4/mcm \leftrightarrow Pbcm$ transition

Comparison of data for CST56 and CST63 (figure 6) reveals that the evolution of tilt angles and strains is barely distinguishable for the $I4/mcm \leftrightarrow Pnma$ and $I4/mcm \leftrightarrow Pbcm$ transitions. There is a small increase in the R_4^+ tilt angle at each of the tetragonal $\leftrightarrow$ orthorhombic transitions while the second tilt, M_3^+ for *Pnma* and T_4 for *Pbcm*, develops discontinuously in the same way for each. The magnitude of the T_4 tilt is, however, slightly greater than the M point tilt. The tetragonal strain, e_{tx}, which scales with the difference in tilt angles (13), is small for both of the orthorhombic structures. The shear strain e_4 is also small in both cases. With respect to tilt and strain aspects, therefore, the *Pnma* and *Pbcm* structures appear to be quite similar. This is also reflected in the only slight difference in trends shown by the two tetragonal $\leftrightarrow$ orthorhombic transition temperatures in the phase diagram (figure 2).

For CST63, the volume strain e_a appears to be continuous through the tetragonal $\leftrightarrow$ orthorhombic transition (figure 5), such that increasing pressure might not affect the relative stability of the $I4/mcm$ and *Pbcm* structures.

5.5. The I4/mcm $\leftrightarrow$ 'mm2' transition

The present study reveals that any anomalies in lattice parameter variations which accompany the low temperature phase transition in Sr-rich samples are at or below the limit of resolution of powder neutron diffraction data for compositions CST90 and CST95. There is a small deflection in e_t for CST90 at ~40 K, but not for CST95 (figure 6) and, perhaps, in e_a for both compositions (figure 5). Note, however, that the variation of e_a is highly sensitive to the

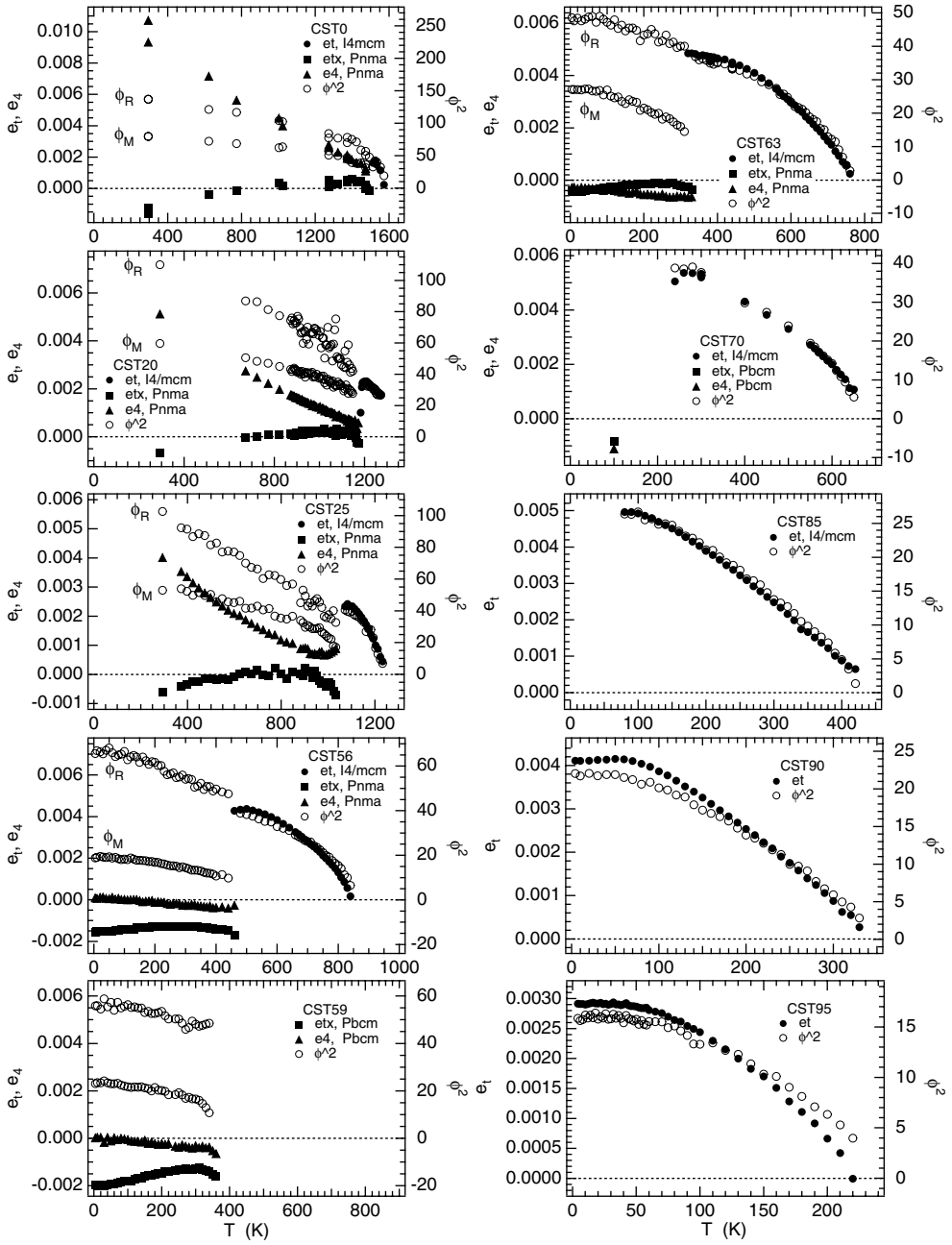

Figure 6. Variation with temperature of the strains of tetragonal and orthorhombic structures (filled symbols, left axis), as extracted from lattice parameters shown in figure 1, in comparison with octahedral tilt angles (open circles, right axis). There are two separate tilt angles in the orthorhombic structures, as defined in section 3.4; these are labelled ϕ_R and ϕ_M for the *Pnma* structure to distinguish between R and M point tilts, respectively, and ϕ_T is the second tilt in *Pbcm* (CST63). The left and right axes have been scaled so that e_t and ϕ^2 data overlap in the stability field of the $I4/mcm$ structure. Data for CST0 are those of Kennedy *et al* (1999) with strains calculated by Carpenter *et al* (2001). R point tilt angles show only a small discontinuity at the tetragonal ↔ orthorhombic transitions.

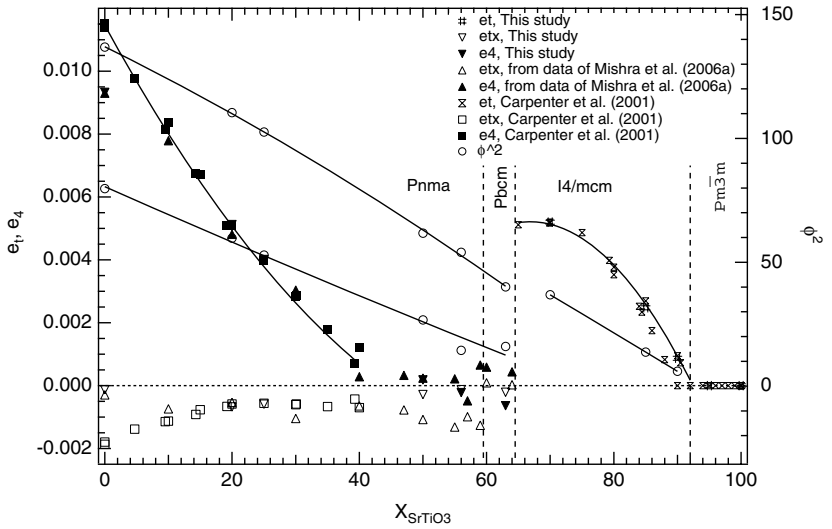

Figure 7. Variations of shear strains (left axis) and tilt angles (open circles, right axis) as a function of composition at room temperature. Boundaries delimiting the *Pnma* and *Pbcm* fields are those given by Mishra *et al* (2006b); the boundary between $I4/mcm$ and cubic stability fields is from Carpenter (2007b). Tilt angles for CST50 were calculated from atomic coordinates obtained by Howard *et al* (2001). Strains referred to as being from Mishra *et al* (2006b) were calculated using lattice parameter data from their figure 8. Lines have been drawn through the data as guides to the eye. Note that e_4 is close to zero in the composition range ∼CST40–CST64, while the tilt angles remain significant at these compositions.

choice of saturation temperature, Θ_s, for a_o in (29). The deflections in lattice parameters found in the present study are smaller than those reported by Mishra *et al* (2005) for CST88, CST94, CST96 and CST98. We have not found any overt evidence for a change from tetragonal to orthorhombic ($mm2$) lattice geometry.

6. Strain and tilt evolution as a function of composition at room temperature

It is well established that orthorhombic CST perovskites with compositions in the range ∼CST40–CST64 differ from other orthorhombic samples at room temperature by having nearly cubic lattice geometry (Ball *et al* 1998, Qin *et al* 2000, Carpenter *et al* 2001, Mishra *et al* 2006b). This is equivalent to the statement that the formal strains e_{tx} and e_4 are small for *Pnma* and *Pbcm* structures in this composition range. The two octahedral tilt angles of these structures do not show any equivalent difference in behaviour, however. Instead, they vary more or less monotonically across the solid solution (figure 7), with essentially the same pattern as shown by their temperature dependences at different compositions (figure 6). The 'nearly cubic' character must arise from a change in the strength of coupling between R point tilting and the shear strain e_4, since e_{tx} is small for all the orthorhombic phases. As shown in figure 7, e_4 reduces steeply from ∼0.001 at CST0 to almost zero at ∼CST40, and then remains small to CST64. In other words, the coupling coefficient λ_5 reduces to almost zero in the CST40–CST64 range. This difference in properties for the two composition ranges of orthorhombic structures at room temperature probably accounts for the difference in effective line widths of hard mode absorption bands in powder absorption IR spectra from samples with the same compositions (Meyer *et al* 2002).

7. Discussion

The topology of the proposed phase diagram (figure 2) is revealing of several general properties of the CST solid solution, while details of tilt angle and strain variations shed further light on the specific properties of samples with intermediate compositions. Firstly, there is clearly a difference in the overall behaviour of samples with compositions CST0–CST85, in comparison with CST85–CST100. In the Ca-rich range the $Pm\bar{3}m \leftrightarrow I4/mcm$ transition is approximately tricritical and can be described using a more or less constant value for the prefactor term of (30), i.e. $16\lambda_4^2 a_2 \Theta_{s2}/((C_{11}^o - C_{12}^o)^2(c_2 + c_2''))$. Moreover, T_c for this transition is close to being a linear function of composition and the second transition is driven predominantly by an octahedral tilting instability. In contrast, the cubic $\leftrightarrow$ tetragonal transition in samples towards the Sr-rich end of the solid solution is marked by changes in slope of T_c with composition, a change from tricritical towards second order character and a change from tilting to ferroelectric displacements as the driving mechanism for the second transition. This is presumably a reflection of geometrical factors as the ratio of cation sizes on the A and B sites changes. The driving energy for a second tilting transition in this system goes to zero at ~CST85–CST87, where it is replaced by a small driving energy for ferroelectric displacements. It should be added that (1) provides a convenient description for the composition dependence of T_c across the entire solid solution but does not discount the possibility that the change in the vicinity of ~CST85–CST90 could be steeper than is implied by the fit shown in figure 2. If the T_c value for CST94 reported by Mishra *et al* (2005) is an outlier, the break in slope need not be at a discrete composition as shown in their figure 6, however.

From the perspective of lattice geometry alone, the cubic $\leftrightarrow$ tetragonal transition is the same across the entire solid solution. If the transition was to an $Imma$ structure in the composition range CST65–CST94, the evolution of lattice parameters and strains would be quite different for samples in this range in comparison with other compositions. All the available data from the literature and from the present study show essentially the same continuous variation through the first transition temperature. In order to reconcile these results for macroscopic properties with the conclusions drawn from Raman spectroscopy by Ouillon *et al* (2002), Ranson *et al* (2005) and Mishra *et al* (2001, 2005, 2006a), it could be argued that the $Imma$ structure in CST65-CST94 is stabilized by some other process than R point tilting. Evidence of this should show up in irregularities of T_{c2} with composition or of the tilt angles with temperature, however. Alternatively, it might be argued that the local symmetry sampled by Raman spectroscopy is lower than the average macroscopic symmetry implied by the lattice geometry determined by powder diffraction. In the same context, structures with $C2/m$ or $P2_1/m$ symmetry might be stable (Woodward *et al* 2006), but they would need to develop without the introduction of any macroscopic strain at the resolution limit of high resolution powder neutron diffraction.

The nearly cubic geometry of intermediate members of the solid solution arises because the apparently normal evolution of tilt angles is not accompanied by a shear strain e_4. This has been ascribed formally here to a composition dependence for the coupling coefficient, λ_5. It is interesting to note that this coefficient does not contribute in any way to the energetics of the $Pm\bar{3}m \leftrightarrow I4/mcm$ transition because it appears in terms with opposite sign in (19) and (20), and the renormalized fourth order coefficient for this transition is $(b_2^* + b_2'^*)$. For silicate solid solutions it has been argued that accommodation of cations with different sizes is achieved by the development of local strain fields as the framework relaxes around the cation sites (Boffa Ballaran *et al* 1998, 1999, 2000, 2001, Atkinson *et al* 1999, Carpenter and Boffa Ballaran 2001, Tarantino *et al* 2002, 2003). Length scales of the resulting local strain heterogeneities have been estimated to be ~5–40 Å (Carpenter 1992, Hayward and Salje 1996, Carpenter *et al* 1999, Boffa

Ballaran *et al* 2000). We propose that the influence of similar heterogeneous strain variations at the length scale of a few unit cells in a perovskite would hinder the development of cooperative distortions which combine over longer distances to cause the macroscopic strain. This is, in effect, a frustration process by which local distortions around a small cation and around a nearby large cation impede longer ranging homogenous strain fields from developing through the whole structure. If this mechanism is correct, a link is established between non-ideal mixing behaviour and phase transition behaviour that depends on local strain. Note that it is the strain coupling which is suppressed and not the phase transition itself, with possible implications for the lattice geometry of other perovskite solid solutions which display diverse transformation behaviour at intermediate compositions (such as $PbTiO_3$–$PbZrO_3$). The ability to suppress strain coupling while not suppressing a phase transition, by manipulation of composition, could also have beneficial consequences for the design of devices in which a shape change associated with switching of twin domains could lead to a mechanical failure.

It has been argued here that the evolution of octahedral tilts in structures with *Pbcm* symmetry is essentially the same as in structures with *Pnma* symmetry. Softening of modes at the M and R points can be accompanied by softening along the entire branch between them (see, e.g., Stirling 1972, Giddy *et al* 1993, Wang *et al* 2000), in which case it is not surprising that the lowest energy state might occasionally be achieved by tilting associated with points between the end points. In this sense, the antiferroelectric character of the *Pbcm* structure could be viewed simply as an accident of symmetry, developing mainly because it is permitted by the particular tilting geometry associated with coupling of R and T point representations. Alternative, but closely related, tilt systems with different multiple repeats along [001] of the parent cubic structure might also turn up in other perovskite solid solutions. An additional factor is the evolution of the volume strain. The onset of tilting is accompanied by a small volume reduction, but increasing the rotation angles brings the A and B cations closer to each other. At some degree of rotation repulsive forces between these cations will begin to dominate and the octahedra would be forced to expand. Perovskite solid solutions at high pressures might display a further diversity of coupled transition mechanisms, therefore. Certainly, a diversity of superstructure types and non-linear variations of transition points in PT space should be anticipated.

CST perovskites show a uniform behaviour of tilt angles with composition and temperature. At each composition the macroscopic strains evolve with the square of the tilt angles, more or less as expected, but the strength of coupling between tilts and specific strains can apparently vary. The properties of hard modes in IR and Raman spectra from this system seem to follow the strains rather than the tilts. This is seen, for example, in the variation of the effective line width parameter $\delta\Delta_{corr}$ reported for IR spectra by Meyer *et al* (2002), and the integrated intensity of a Raman band at 150–175 cm^{-1} reported by Qin *et al* (2002, their figure 3), which both scale with e_4 in orthorhombic structures at room temperature. Hard mode spectroscopy (Bismayer 1990, Salje 1992, 1994, Salje and Bismayer 1997, Salje *et al* 2000) is effectively as much a probe of the strength of strain/order parameter coupling as it is of the evolution of the order parameter, therefore. The elastic strain behaviour of perovskites, as revealed by examination of the evolution of symmetry-adapted macroscopic strains, clearly plays an important role in determining both static and dynamic properties.

Acknowledgments

The authors thank Mr Ian Watson, Mr Gordon Thorogood and Ms Melody Carter of the Australian Nuclear Science and Technology Organisation (ANSTO) for the preparation of

samples for this study, and Dr Cliff Ball, ANSTO, for making available samples used in his earlier work. The assistance of Dr Richard Ibberson, ISIS Facility, Dr Keiichi Osaka from SPring-8, and Dr Brendan Kennedy and Mr Paul Saines of the University of Sydney, through what has been a long programme of measurements, is gratefully acknowledged. The neutron facilities at ISIS are operated by the Council for the Central Laboratories of the Research Councils (CCLRC), with a contribution from the Australian Research Council. Travel by CJH and ZZ to ISIS and SPring-8 was funded by the Commonwealth of Australia under the Access to Major Research Facilities Program. Studies of perovskites are currently supported by the Australian Research Council, grant DP055722.

References

Ali R and Yashima M 2005 Space group and crystal structure of the perovskite $CaTiO_3$ from 296 to 1720 K *J. Solid State Chem.* **178** 2867–72

Atkinson A J, Carpenter M A and Salje E K H 1999 Hard mode spectroscopy of plagioclase feldspars *Eur. J. Mineral.* **11** 7–21

Ball C J, Begg B D, Cookson D J, Thorogood G J and Vance E R 1998 Structures in the system $CaTiO_3/SrTiO_3$ *J. Solid State Chem.* **139** 238–47

Bednorz J G and Müller K A 1984 $Sr_{1-x}Ca_xTiO_3$: An XY quantum ferroelectric with transition to randomness *Phys. Rev. Lett.* **52** 2289–92

Bianchi U 1996 *PhD Thesis* Gerhard-Marcator Universität, Duisburg

Bianchi U, Dec J, Kleemann W and Bednorz J G 1995 Cluster and domain-state dynamics of ferroelectric $Sr_{1-x}Ca_xTiO_3$ ($x = 0.007$) *Phys. Rev.* B **51** 8737–46

Bianchi U, Kleemann W and Bednorz J G 1994a Ferroelectric domain state transition of $SrTiO_3$:Ca *Ferroelectrics* **157** 165–70

Bianchi U, Kleemann W and Bednorz J G 1994b Raman scattering of ferroelectric $Sr_{1-x}Ca_xTiO_3$, $x = 0.007$ *J. Phys.: Condens. Matter* **6** 1229–38

Bismayer U 1990 Hard mode Raman spectroscopy and its applications to ferroelastic and ferroelectric phase transitions *Phase Transit.* **27** 211–67

Boffa Ballaran T, Angel R J and Carpenter M A 2000 High-pressure transformation behaviour of the cummingtonite–grunerite solid solution *Eur. J. Mineral.* **12** 1195–213

Boffa Ballaran T, Carpenter M A, Domeneghetti M C, Salje E K H and Tazzoli V 1998 Structural mechanisms of solid solution and cation ordering in augite–jadeite pyroxenes: II. A microscopic perspective *Am. Mineral.* **83** 434–43

Boffa Ballaran T, Carpenter M A, Geiger C A and Koziol A M 1999 Local structural heterogeneity in garnet solid solutions *Phys. Chem. Minerals* **26** 554–69

Boffa Ballaran T, Carpenter M A and Ross N L 2001 Infrared powder-absorption spectroscopy of Ca-free $P2_1/c$ clinopyroxenes *Min. Mag.* **65** 339–50

Bulou A, Rousseau M and Nouet J 1992 Ferroelastic phase transitions and related phenomena *Key Eng. Mater.* **68** 133–86

Carpenter M A 1992 Thermodynamics of phase transitions in minerals: a macroscopic approach *The Stability of Minerals* ed G D Price and N L Ross (London: Chapman and Hall) pp 172–215

Carpenter M A 2007a Elastic anomalies accompanying phase transitions in (Ca, Sr)TiO_3 perovskites I: Landau theory and a calibration for $SrTiO_3$ *Am. Mineral.* at press

Carpenter M A 2007b Elastic anomalies accompanying phase transitions in (Ca, Sr)TiO_3 perovskites II: calibration for the effects of composition and pressure *Am. Mineral.* at press

Carpenter M A, Becerro A I and Seifert F 2001 Strain analysis of phase transitions in (Ca, Sr)TiO_3 perovskites *Am. Mineral.* **86** 348–63

Carpenter M A and Boffa Ballaran T 2001 The influence of elastic strain heterogeneities in silicate solid solutions *EMU Notes Mineral.* **3** 155–78

Carpenter M A, Boffa Ballaran T and Atkinson A J 1999 Microscopic strain, local structural heterogeneity and the energetics of silicate solid solutions *Phase Transit.* **69** 95–109

Carpenter M A, Howard C J, Kennedy B J and Knight K S 2005 Strain mechanism for order-parameter coupling through successive phase transitions in $PrAlO_3$ *Phys. Rev.* B **72** 024118

Carpenter M A, Li B and Liebermann R C 2007 Elastic anomalies accompanying phase transitions in (Ca, Sr)TiO_3 perovskites III: experimental investigation of polycrystalline samples *Am. Mineral.* at press

Carpenter M A, Meyer H-W, Sondergeld P, Marion S and Knight K S 2003 Spontaneous strain variations through the low temperature phase transitions of deuterated lawsonite *Am. Mineral.* **88** 534–46

Ceh M, Kolar D and Golic L 1987 The phase diagram of $CaTiO_3$–$SrTiO_3$ *J. Solid State Chem.* **68** 68–72

Cowley R A, Buyers W J L and Dolling G 1969 Relationship of normal modes of vibration of strontium titanate and its antiferroelectric phase transition at 110 K *Solid State Commun.* **7** 181–4

Fossheim K and Berre B 1972 Ultrasonic propagation, stress effects, and interaction parameters at the displacive transition in $SrTiO_3$ *Phys. Rev.* B **5** 3292–308

Gallardo M C, Becerro A I, Romero F J, del Cerro J, Seifert F and Redfern S A T 2003 Cubic–tetragonal phase transition in $Ca_{0.04}Sr_{0.96}TiO_3$: a combined specific heat and neutron diffraction study *J. Phys.: Condens. Matter* **15** 91–100

Giddy A P, Dove M T, Pawley G S and Heine V 1993 The determination of rigid-unit-modes as potential soft modes for displacive phase transitions in framework crystal structures *Acta Crystallogr.* A **49** 697–703

Gillet P, Guyot F, Price G D, Tournerie B and Le Cleach A 1993 Phase changes and thermodynamic properties of $CaTiO_3$. Spectroscopic data, vibrational modelling and some insights on the properties of $MgSiO_3$ perovskite *Phys. Chem. Minerals* **20** 159–70

Glazer A M 1972 The classification of tilted octahedra in perovskites *Acta Crystallogr.* B **28** 3384–92

Glazer A M 1975 Simple ways of determining perovskite structures *Acta Crystallogr.* A **31** 756–62

Gränicher H and Jakits O 1954 Über die dielektrischen Eigenschaften und Phasenumwandlungen bei Mischkristallsystemen vom Perowskittyp *Nuovo Cimento* **9** (Suppl.) 480–520

Guyot F, Richet P, Courtial Ph and Gillet Ph 1993 High-temperature heat capacity and phase transitions of $CaTiO_3$ perovskite *Phys. Chem. Minerals* **20** 141–6

Harrison R J, Redfern S A T and Street J 2003 The effect of transformation twins on the seismic-frequency mechanical properties of polycrystalline $Ca_{1-x}Sr_xTiO_3$ perovskite *Am. Mineral.* **88** 574–82

Hayward S A, Morrison F D, Redfern S A T, Salje E K H, Scott J F, Knight K S, Tarantino S, Glazer A M, Shuvaeva V, Daniel P, Zhang M and Carpenter M A 2005 Transformation processes in $LaAlO_3$: neutron diffraction, dielectric, thermal, optical and Raman studies *Phys. Rev.* B **72** 054110

Hayward S A and Salje E K H 1996 Displacive phase transition in anorthoclase: the plateau effect and the effect of T1–T2 ordering on the transition temperature *Am. Mineral.* **81** 1332–6

Hayward S A and Salje E K H 1998 Low-temperature phase diagrams: non-linearities due to quantum mechanical saturation of order parameters *J. Phys.: Condens. Matter* **10** 1421–30

Hayward S A and Salje E K H 1999 Cubic–tetragonal phase transition in $SrTiO_3$ revisited: Landau theory and transition mechanism *Phase Transit.* **68** 501–22

Hirata T, Ishioka K and Kitajima M 1996 Vibrational spectroscopy and x-ray diffraction of perovskite compounds $Sr_{1-x}M_xTiO_3$ ($M = Ca, Mg$; $0 \leqslant x \leqslant 1$) *J. Solid State Chem.* **124** 353–9

Howard C J, Knight K S, Kennedy B J and Kisi E H 2000 The structural phase transitions in strontium zirconate revisited *J. Phys.: Condens. Matter* **12** L677–83

Howard C J, Lumpkin G R, Smith R I and Zhang Z 2004 Crystal structures and phase transition in the system $SrTiO_3$–$La_{2/3}TiO_3$ *J. Solid State Chem.* **177** 2726–32

Howard C J and Stokes H T 1998 Group-theoretical analysis of octahedral tilting in perovskites *Acta Crystallogr.* B **54** 782–9

Howard C J and Stokes H T 2005 Structures and phase transitions in perovskites—a group theoretical approach *Acta Crystallogr.* A **61** 93–111

Howard C J, Withers R L and Kennedy B J 2001 Space group and structure for the perovskite $Ca_{0.5}Sr_{0.5}TiO_3$ *J. Solid State Chem.* **160** 8–12

Howard C J, Withers R L, Knight K S and Zhang Z 2006 $Ca_{0.37}Sr_{0.63}TiO_3$ perovskite: an example of an unusual class of tilted perovskites, in preparation

Howard C J, Withers R L, Zhang Z, Osaka K, Kato K and Takata M 2005 Space-group symmetry for the perovskite $Ca_{0.3}Sr_{0.7}TiO_3$ *J. Phys.: Condens. Matter* **17** L459–65

Ibberson R M, David W I F and Knight K S 1992 The high resolution neutron powder diffractometer (HRPD) at ISIS—a user guide *Report* RAL-92-031

Kennedy B J, Howard C J and Chakoumakos B C 1999 Phase transitions in perovskite at elevated temperatures—a powder neutron diffraction study *J. Phys.: Condens. Matter* **11** 1479–88

Kennedy B J, Howard C J, Knight K S, Zhang Z and Zhou Q 2006 Structures and phase transitions in the ordered double perovskites $Ba_2Bi^{III}Bi^{V}O_6$ and $Ba_2Bi^{III}Sb^{V}O_6$ *Acta Crystallogr.* B **62** 537–46

Kityk A V, Schranz W, Sondergeld P, Havlik D, Salje E K H and Scott J F 2000a Low-frequency superelasticity and nonlinear elastic behavior in $SrTiO_3$ crystals *Phys. Rev.* B **61** 946–56

Kityk A V, Schranz W, Sondergeld P, Havlik D, Salje E K H and Scott J F 2000b Nonlinear elastic behaviour of $SrTiO_3$ crystals in the quantum paraelectric regime *Europhys. Lett.* **50** 41–7

Kleemann W, Albertini A, Kuss M and Lindner R 1997 Optical detection of symmetry breaking on a nanoscale in $SrTiO_3$:Ca *Ferroelectrics* **203** 57–64

Kleemann W, Bianchi U, Bürgel A, Prasse M and Dec J 1995 Domain state properties of weakly doped $SrTiO_3$:Ca *Phase Transit.* **55** 57–68

Larson A C and Von Dreele R B 2000 General structure analysis system (GSAS) Los Alamos National Laboratory *Report* LAUR 86–748

Laubereau A and Zurek R 1970 Brillouin–Streuung in Strontiumtitanit–Einkristallen im Temperaturbereich 5 K bis 300 K *Z. Naturf.* a **25** 391–401

Lemanov V V 1997 Phase transitions in $SrTiO_3$-based solid solutions *Phys. Solid State* **39** 1468–73

Liu M, Finlayson T R and Smith T F 1997 High-resolution dilatometry measurements of $SrTiO_3$ along cubic and tetragonal axes *Phys. Rev.* B **55** 3480–4

Liu X and Liebermann R C 1993 X-ray powder diffraction study of $CaTiO_3$ perovskite at high temperatures *Phys. Chem. Minerals* **20** 171–5

Lüthi B and Moran T J 1970 Sound propagation near the structural phase transition in strontium titanate *Phys. Rev.* B **2** 1211–4

McQuarrie M 1955 Structural behavior in the system $(Ba, Ca, Sr)TiO_3$ and its relation to certain dielectric characteristics *J. Am. Ceram. Soc.* **38** 444–9

Meyer H-W, Carpenter M A, Becerro A I and Seifert F 2002 Hard-mode infrared spectroscopy of perovskites across the $CaTiO_3$–$SrTiO_3$ solid solution *Am. Mineral.* **87** 1291–6

Meyer H-W, Carpenter M A, Graeme-Barber A, Sondergeld P and Schranz W 2000 Local and macroscopic order parameter variations associated with low temperature phase transitions in lawsonite, $CaAl_2Si_2O_7(OH)_2{\cdot}H_2O$ *Eur. J. Mineral.* **12** 1139–50

Meyer H-W, Marion S, Sondergeld P, Carpenter M A, Knight K S, Redfern S A T and Dove M T 2001 Displacive components of the low-temperature phase transitions in lawsonite *Am. Mineral.* **86** 566–77

Mishra S K, Ranjan R, Pandey D and Kennedy B J 2002 Powder neutron diffraction study of the antiferroelectric phase transition in $Sr_{0.75}Ca_{0.25}TiO_3$ *J. Appl. Phys.* **91** 4447–52

Mishra S K, Ranjan R, Pandey D, Ouillon R, Pinan-Lucarre J-P, Ranson P and Pruzan Ph 2001 A Raman scattering study of the antiferrroelectric phase transition in $(Sr_{0.70}Ca_{0.30})TiO_3$ *Phys. Rev.* B **64** 092302

Mishra S K, Ranjan R, Pandey D, Ranson P, Ouillon R, Pinan-Lucarre J-P and Pruzan Ph 2005 A combined x-ray diffraction and Raman scattering study of the phase transitions in $Sr_{1-x}Ca_xTiO_3$ ($x = 0.04, 0.06, 0.12$) *J. Solid State Chem.* **178** 2846–57

Mishra S K, Ranjan R, Pandey D, Ranson P, Ouillon R, Pinan-Lucarre J-P and Pruzan Ph 2006a Resolving the controversies about the 'nearly cubic' and other phases of $Sr_{1-x}Ca_xTiO_3$ ($0 \leqslant x \leqslant 1$): II Comparison of phase transition behaviours for $x = 0.40$ and 0.43 *J. Phys.: Condens. Matter* **18** 1899–912

Mishra S K, Ranjan R, Pandey D and Stokes H T 2006b Resolving the controversies about the 'nearly cubic' and other phases of $Sr_{1-x}Ca_xTiO_3$ ($0 \leqslant x \leqslant 1$): I. Room temperature structures *J. Phys.: Condens. Matter* **18** 1885–98

Mitsui T and Westphal W B 1961 Dielectric and x-ray studies of $Ca_xBa_{1-x}TiO_3$ and $Ca_xSr_{1-x}TiO_3$ *Phys. Rev.* **124** 1354–9

Müller K A and Berlinger W 1971 Static critical exponents at structural phase transitions *Phys. Rev. Lett.* **26** 13–6

Müller K A, Berlinger W and Tosatti E 1991 Indication for a novel phase in the quantum paraelectric regime of $SrTiO_3$ *Z. Phys.* B **84** 277–83

Okai B and Yoshimoto J 1975 Pressure dependence of the structural phase transition temperature in $SrTiO_3$ and $KMnF_3$ *J. Phys. Soc. Japan* **39** 162–5

Okazaki A and Kawaminami M 1973 Lattice constant of strontium titanate at low temperatures *Mater. Res. Bull.* **8** 545–50

Ouillon R, Pinan-Lucarre J-P, Ranson P, Pruzan Ph, Mishra S K, Ranjan R and Pandey D 2002 A Raman scattering study of the phase transitions in $SrTiO_3$ and in the mixed system $(Sr_{1-x}Ca_x)TiO_3$ at ambient pressure from $T = 300$ K down to 8 K *J. Phys.: Condens. Matter* **14** 2079–92

Qin S, Becerro A I, Seifert F, Gottsmann J and Jiang J 2000 Phase transitions in $Ca_{1-x}Sr_xTiO_3$ perovskites: effects of composition and temperature *J. Mater. Chem.* **10** 1609–15

Qin S, Wu X, Seifert F and Becerro A I 2002 Micro-Raman study of perovskites in the $CaTiO_3$–$SrTiO_3$ system *J. Chem. Soc., Dalton Trans.* **2002** 3751–5

Ranjan R and Pandey D 1999 Novel structural features and phase transition behaviour of $(Sr_{1-x}Ca_x)TiO_3$: II. X-ray diffraction studies *J. Phys.: Condens. Matter* **11** 2247–58

Ranjan R and Pandey D 2001a Antiferroelectric phase transition in $(Sr_{1-x}Ca_x)TiO_3$ ($0.12 \leqslant x \leqslant 0.40$): I. Dielectric studies *J. Phys.: Condens. Matter* **13** 4239–49

Ranjan R and Pandey D 2001b Antiferroelectric phase transition in $(Sr_{1-x}Ca_x)TiO_3$: II. X-ray diffraction studies *J. Phys.: Condens. Matter* **13** 4251–66

Ranjan R, Pandey D and Lalla N P 2000 Novel features of $Sr_{1-x}Ca_xTiO_3$ phase diagram: evidence for competing antiferroelectric and ferroelectric interactions *Phys. Rev. Lett.* **84** 3726–9

Ranjan R, Pandey D, Schuddinck W, Richard O, De Meulenaere P, Van Landuyt J and Van Tendeloo G 2001 Evolution of crystallographic phases in $(Sr_{1-x}Ca_x)TiO_3$ with composition (x) *J. Solid State Chem.* **162** 20–8

Ranjan R, Pandey D, Siruguri V, Krishna P S R and Paranjpe S K 1999 Novel structural features and phase transition behaviour of $(Sr_{1-x}Ca_x)TiO_3$: I. Neutron diffraction study *J. Phys.: Condens. Matter* **11** 2233–46

Ranson P, Ouillon R, Pinan-Lucarre J-P, Pruzan Ph, Mishra S K, Ranjan R and Pandey D 2005 The various phases of the system $Sr_{1-x}Ca_xTiO_3$—a Raman scattering study *J. Raman Spectrosc.* **36** 898–911

Redfern S A T 1996 High-temperature structural phase transitions in perovskite ($CaTiO_3$) *J. Phys.: Condens. Matter* **8** 8267–75

Rehwald W 1970a Anomalous ultrasonic attenuation at the 105 K transition in strontium titanate *Solid State Commun.* **8** 607–11

Rehwald W 1970b Low temperature elastic moduli of strontium titanate *Solid State Commun.* **8** 1483–5

Rietveld H M 1969 A profile refinement method for nuclear and magnetic structures *J. Appl. Crystallogr.* **2** 65–71

Ringwood A E, Kesson S E, Reeve K D, Levins D M and Ramm E J 1988 *Synroc Radioactive Waste Forms for the Future* ed W Lutze and R C Ewing (Amsterdam: North-Holland) pp 233–334

Salje E K H 1992 Hard-mode spectroscopy: experimental studies of structural phase transitions *Phase Transit.* **37** 83–110

Salje E K H 1994 Phase transitions and vibrational spectroscopy in feldspars *Feldspars and their Reactions* (*NATO ASI ser. C* vol 421) ed I Parsons (Dordrecht: Kluwer) pp 103–60

Salje E K H and Bismayer U 1997 Hard mode spectroscopy: the concept and applications *Phase Transit.* **63** 1–75

Salje E K H, Carpenter M A, Malcherek T and Boffa Ballaran T 2000 Autocorrelation analysis of infrared spectra from minerals *Eur. J. Mineral.* **12** 503–19

Salje E K H, Gallardo M C, Jiménez J, Romero F J and del Cerro J 1998 The cubic–tetragonal phase transition in strontium titanite: excess specific heat measurements and evidence for a near-tricritical, mean field type transition mechanism *J. Phys.: Condens. Matter* **10** 5535–43

Salje E K H, Wruck B and Thomas H 1991 Order-parameter saturation and low-temperature extension of Landau theory *Z. Phys.* B **82** 399–404

Sasaki S, Prewitt C T, Bass J D and Schulze W A 1987 Orthorhombic perovskite $CaTiO_3$ and $CdTiO_3$: crystal structure and space group *Acta Crystallogr.* C **43** 1668–74

Schranz W, Sondergeld P, Kityk A V and Salje E K H 1999 Elastic properties of $SrTiO_3$ crystals at ultralow frequencies *Phase Transit.* **69** 61–76

Shirane G and Yamada Y 1969 Lattice-dynamical study of the 110 K phase transition in $SrTiO_3$ *Phys. Rev.* **177** 858–63

Slonczewski J C and Thomas H 1970 Interaction of elastic strain with the structural transition of strontium titanate *Phys. Rev.* B **1** 3599–608

Sondergeld P, Schranz W, Kityk A V, Carpenter M A and Libowitzky E 2000 Ordering behaviour of the mineral lawsonite *Phase Transit.* **71** 189–203

Stirling W G 1972 Neutron inelastic scattering study of the lattice dynamics of strontium titanate: harmonic models *J. Phys. C: Solid State Phys.* **5** 2711–30

Tarantino S C, Boffa Ballaran T, Carpenter M A, Domeneghetti M C and Tazzoli V 2002 Mixing properties of the enstatite–ferrosilite solid solution: II. A microscopic perspective *Eur. J. Mineral.* **14** 537–47

Tarantino S C, Carpenter M A and Domeneghetti M C 2003 Strain and local heterogeneity in the forsterite–fayalite solid solution *Phys. Chem. Minerals* **30** 495–502

Toby B H 2001 EXPGUI, a graphical user interface for GSAS *J. Appl. Crystallogr.* **34** 210–3

Unoki H and Sakudo T 1967 Electron spin resonance of Fe^{3+} in $SrTiO_3$ with special reference to the 110 K phase transition *J. Phys. Soc. Japan* **23** 546–52

Vanderbilt D and Cohen M H 2001 Monoclinic and triclinic phases in higher-order Devonshire theory *Phys. Rev.* B **63** 094108

Wang R, Zhu Y and Shapiro S M 2000 Electron diffraction studies of phonon and static disorder in $SrTiO_3$ *Phys. Rev.* B **61** 8814–22

Woodward D I, Wise P L, Lee W E and Reaney I M 2006 Space group symmetry of $(Ca_xSr_{1-x})TiO_3$ determined using electron diffraction *J. Phys.: Condens. Matter* **18** 2401–8

Worlock J M, Scott J F and Fleury P A 1969 Soft phonon modes and the 110 K phase transition in $SrTiO_3$ *Light Scattering of Solids* ed G B Wright (New York: Springer) pp 689–96

Yamanaka T, Hirai N and Komatsu Y 2002 Structure change of $Ca_{1-x}Sr_xTiO_3$ perovskite with composition and pressure *Am. Mineral.* **87** 1183–9